

CompMarkGS: Robust Watermarking for Compression 3D Gaussian Splatting

Sumin In¹ Youngdong Jang¹ Utae Jeong¹ MinHyuk Jang¹ Hyeongcheol Park¹
Eunbyung Park² Sangpil Kim^{1*}

¹Korea University ²Yonsei University

{ism0705, altu1996, utaejeong, wkdalsgur85, broiron, spk7}@korea.ac.kr epark@yonsei.ac.kr

Abstract

3D Gaussian Splatting (3DGS) enables rapid differentiable rendering for 3D reconstruction and novel view synthesis, leading to its widespread commercial use. Consequently, copyright protection via watermarking has become critical. However, because 3DGS relies on millions of Gaussians, which require gigabytes of storage, efficient transfer and storage require compression. Existing 3DGS watermarking methods are vulnerable to quantization-based compression, often resulting in the loss of the embedded watermark. To address this challenge, we propose a novel watermarking method that ensures watermark robustness after model compression while maintaining high rendering quality. In detail, we incorporate a quantization distortion layer that simulates compression during training, preserving the watermark under quantization-based compression. Also, we propose a learnable watermark embedding feature that embeds the watermark into the anchor feature, ensuring structural consistency and seamless integration into the 3D scene. Furthermore, we present a frequency-aware anchor growing mechanism to enhance image quality in high-frequency regions by effectively identifying Gaussians within these regions. Experimental results confirm that our method preserves the watermark and maintains superior image quality under high compression, validating it as a promising approach for a secure 3DGS model.

1. Introduction

3D Gaussian Splatting (3DGS) [15] has emerged as a powerful technique for high-quality real-time 3D rendering and is increasingly adopted across various industries, including AR/VR, 3D animation, and gaming. With the widespread adoption of 3DGS in commercial applications, protecting the copyright of the 3DGS model itself has become a critical issue, leading to growing interest in copyright protection, particularly watermarking techniques for 3DGS mod-

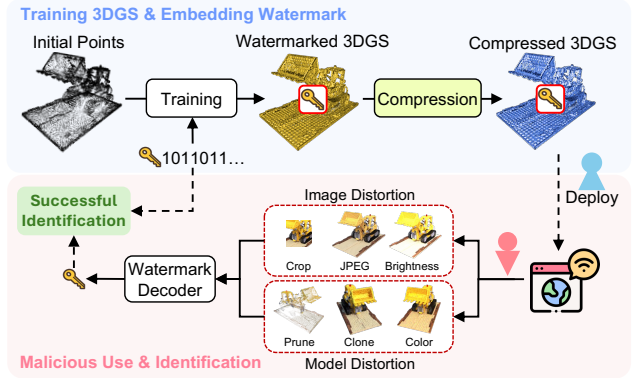


Figure 1. A model watermarked with the proposed method, CompMarkGS, can protect its copyright from unauthorized users when deployed across various digital environments after compression.

els [6, 9, 11, 49]. A major limitation of 3DGS is its reliance on a large number of 3D Gaussians to accurately represent complex objects and large-scale scenes, which demands substantial storage space. Therefore, model compression is crucial for the storage and transmission of 3DGS models. However, the integration of model compression [4, 40] and watermark embedding techniques for 3DGS is significantly challenging and has not been extensively explored.

To the best of our knowledge, no existing work successfully achieves both watermark embedding and model compression for 3DGS models while preserving high rendering quality, as illustrated in Fig.1. Embedding a watermark requires modifying 3D Gaussian parameters, such as adding or removing Gaussians. Additionally, the compression process also involves modifications. These changes can impact rendering quality, making the task even more challenging. The sparse and unstructured nature of Gaussian point clouds further complicates the development of a specialized approach that embeds robust watermarks into 3DGS models while enabling efficient compression, ensuring copyright protection without compromising rendering quality.

We note that the main reason for the failure of 3DGS watermarking in model compression is their vulnerability

*Corresponding author

to the quantization compression stage, resulting in a significant drop in bit accuracy (see Tab.1). To tackle this limitation, we introduce a quantization distortion layer that injects quantization noise during 3DGS model training, enabling the model to pre-adapt to quantization operations. This approach ensures the retention of watermark information during compression, preserving both robust watermark durability and high visual quality after quantization compression.

The proposed method, CompMarkGS, is inspired by anchor-based compression techniques, achieving the highest compression rate and efficiency while preserving high rendering quality. We seamlessly embed watermark messages into the anchor feature using a learnable watermark embedding feature without modifying the original model architecture. Additionally, we introduce a frequency-aware anchor growing mechanism to minimize rendering quality degradation caused by embedding a watermark into the 3DGS model. Specifically, we identify high-frequency regions in the rendered image, align them with the coordinates of neural Gaussians, and apply anchor growing only to these regions. This mechanism enhances the fidelity of fine details, such as edges and textures, thereby improving the overall visual quality and details after watermarking.

We conducted extensive experiments demonstrating that our proposed method preserves watermark integrity and image quality more effectively before and after compression compared to existing methods. Furthermore, our approach exhibits robust performance against both image and model distortions, outperforming existing state-of-the-art techniques across various message bit lengths.

Our main contributions are as follows:

- We propose a watermarking method with compression capability for 3DGS, leveraging an anchor-based compression approach, which is the first method to embed watermarks in anchor-based 3DGS, ensuring compression performance. We achieve state-of-the-art performance.
- We develop a quantization distortion layer to preserve the watermark after quantization-based compression, ensuring high rendering quality and robustness against various watermark attacks.
- We present a novel frequency-aware anchor growing mechanism that selectively enhances high-frequency regions, preserving fine details and minimizing distortion during watermark embedding.
- We introduce an approach that adds watermark embedding to anchor feature parameter while jointly optimizing them with image and message loss, improving robustness against model distortion.

2. Related Work

3D Gaussian Splatting Representation. 3D Gaussian Splatting (3DGS) [15] is an innovative technique for 3D

representation that employs explicit primitives to model 3D worlds. It renders images by projecting these primitives onto target viewpoints and leveraging an α -blender to integrate pixel colors seamlessly. This approach produces high-quality results and significantly enhances real-time rendering performance. Thanks to these advantages, 3DGS has been widely adopted across various research areas, including avatars [1, 27, 29, 33, 47], dynamic scenes [12, 19, 20, 43, 51], and 3D generation [5, 21, 36, 45, 46]. Recently, Scaffold-GS [22] has advanced the 3DGS framework by introducing anchor points to construct a hierarchical 3D representation. Anchor-based methods [7, 18, 34, 41, 48] effectively minimize redundant Gaussians, enhancing rendering quality and increasing robustness against view changes. These representations are promising for optimizing 3DGS compression, achieving both parameter reduction and improved rendering quality.

3D Gaussian Splatting Compression. To achieve high-quality results, 3DGS generates a large number of Gaussians, which leads to significant storage overhead. To address the storage overhead, vector quantization methods [8, 17, 30, 31, 39, 44] have been widely explored. These methods prune Gaussians with minimal impact on rendering quality and use codebooks to compactly encode the attributes of Gaussians. More recently, anchor-based representations have gained significant attention in 3DGS, such as Scaffold-GS [22]. Compression methods that leverage the structural relationships between anchors have shown state-of-the-art performance. For example, HAC [4] reduces spatial redundancies among anchors by utilizing hash grids for parameter quantization and enabling entropy modeling. ContextGS [40] introduces a unified compression framework with a factorized prior, enabling entropy modeling of anchor features while leveraging hierarchical anchor relations to reduce redundancy among anchors. Given their compression efficiency, anchor-based representations are especially advantageous for real-world applications.

Digital Watermarking. To protect the copyright of digital assets, digital watermarking has been studied over the decades. Deep learning-based watermarking [13, 23, 35, 50] employs an encoder-decoder architecture, and it has shown competitive performance in terms of robustness against various distortions compared to traditional watermarking methods in the pixel domain [38, 42] and the frequency domain [2, 14, 16, 28, 32, 37]. Recently, digital watermarking has been integrated with radiance field models, such as NeRF [26] and 3DGS [15], to protect the copyrights of both the models and their 3D-generated content. For example, CopyRNeRF [24] is the first digital watermarking method for implicit NeRF, introducing a watermarked color representation. WateRF [10] is a plug-and-play method compatible with all radiance field representations, leveraging the frequency domain to achieve robust

watermarking. GaussianMarker [9] embeds the watermark by estimating the uncertainties of Gaussians and incorporating watermark-specific Gaussians into the existing model based on these uncertainties. 3D-GSW [11] achieves watermark embedding by selectively pruning Gaussians with minimal impact on rendering quality. However, model compression often leads to watermark loss, and robust watermarking methods against compression remain underexplored. Therefore, our work integrates 3DGS training with watermark embedding, ensuring robustness against degradations introduced by model compression.

3. Preliminary

3D Gaussian Splatting. 3D Gaussian Splatting [15] is a method that optimizes scene representation for high-quality novel view synthesis using explicit 3D Gaussian primitives:

$$G(x) = e^{-\frac{1}{2}(x-\mu)^\top \Sigma^{-1}(x-\mu)}, \quad (1)$$

where $x \in \mathbb{R}^3$ is a point in the 3D scene, $\mu \in \mathbb{R}^3$ is the mean, and $\Sigma \in \mathbb{R}^{3 \times 3}$ is the covariance matrix, factorized as $\Sigma = RSS^\top R^\top$ with a scaling matrix $S \in \mathbb{R}^{3 \times 3}$ and a rotation matrix $R \in \mathbb{R}^{3 \times 3}$. For rendering, each 3D Gaussian is projected onto the 2D image, and the pixel color C is rendered by blending the contributions of N ordered points:

$$C = \sum_{i=1}^N c_i \alpha_i \prod_{j=1}^{i-1} (1 - \alpha_j), \quad (2)$$

where $c_i \in \mathbb{R}^3$ and $\alpha_i \in \mathbb{R}^3$ denote the color and opacity assigned to the point. As a result, the learnable parameters, such as position, size, opacity, and color, are optimized to closely match the input views. For more details, we refer the reader to original paper [15].

Scaffold-GS. Scaffold-GS [22] clusters adjacent Gaussians using anchor points, reducing redundancy. Initial anchor points are placed at voxel centers, and each anchor is equipped with a local context feature $f \in \mathbb{R}^d$, scaling factor $l \in \mathbb{R}^3$, and K learnable offsets $O \in \mathbb{R}^{K \times 3}$. Visible anchor points within the viewing frustum generate K Neural Gaussians, with their positions computed as follows:

$$\mu_k = x_a + O_k \odot l, \quad (3)$$

where $x_a \in \mathbb{R}^3$ is the anchor point position, $O_k \in \mathbb{R}^3$ denotes the k -th offset vector, μ_k is the generated k -th Gaussian position, and \odot represents the element-wise product. Each Gaussian's attributes are predicted using separate MLPs:

$$\{c_i, r_i, s_i, \alpha_i\}_{i=1}^K = \text{MLP}(f, \delta_{av}, \vec{d}_{av}), \quad (4)$$

where $\delta_{av} = \|x_a - x_v\|_2$ and $\vec{d}_{av} = \frac{x_a - x_v}{\|x_a - x_v\|_2}$ denote the relative viewing distance and direction between the camera

(x_v) and the anchor (x_a) positions. The Gaussian positions are computed by adding the learnable offsets O_k to the anchor positions, yielding a more compact 3D representation.

4. Method

The overall pipeline of CompMarkGS is shown in Fig.2, inspired by anchor-based compression models. Anchor-based 3DGS compression is one of the most efficient compression methods. The pipeline consists of anchor attributes, a quantization distortion layer, and a frequency-aware anchor growing mechanism, ensuring high rendering quality with robust bit accuracy, as shown in Fig.3. Each components are explained in detail in this section.

4.1. Anchor-based 3DGS Watermarking

We embed the watermark in one of the attributes of each anchor, namely the anchor feature. Unlike vanilla 3DGS [11], which represents a 3D scene using individual Gaussian primitives, anchor-based 3DGS dynamically predicts Gaussian attributes based on anchor points. In CompMarkGS, the anchor feature encodes both local scene information to guide the dynamic prediction of Gaussian attributes. Although the anchor feature f indirectly influences Gaussian attributes through its input to the MLPs, parameters such as scaling l and offsets O directly control the position, size, and shape of the Gaussians. Direct watermark insertion into these parameters leads to significant structural distortions and degraded rendering quality, as shown in Fig.3. To preserve structural consistency and seamlessly integrate the watermark into the 3D scene, we embed the watermark in the anchor feature. To achieve this, we employ a learnable watermark embedding feature. Specifically, the watermark embedding feature $f' \in \mathbb{R}^d$ has the same dimension as the anchor feature $f \in \mathbb{R}^d$, and the watermarked feature is defined as follows:

$$f^w = f + \tanh(f'), \quad \text{where } f, f' \in \mathbb{R}^d, \quad (5)$$

where $\tanh(\cdot)$ represents the element-wise hyperbolic tangent function. To prevent the watermark embedding feature from growing excessively, we use $\tanh(\cdot)$ to constrain its values to the range of $[-1, 1]$ before adding it to the anchor feature. The watermark embedding feature is a learnable parameter that is integrated into the anchor feature and trained to maintain the watermark without compromising the quality of the 3D scene.

4.2. Robustness for Quantization

Our goal is to ensure that the watermarked model retains its watermark information after the model compression. Since many compression methods rely on quantization, we incorporate a quantization compression distortion layer to optimize watermark retention during compression. To be more

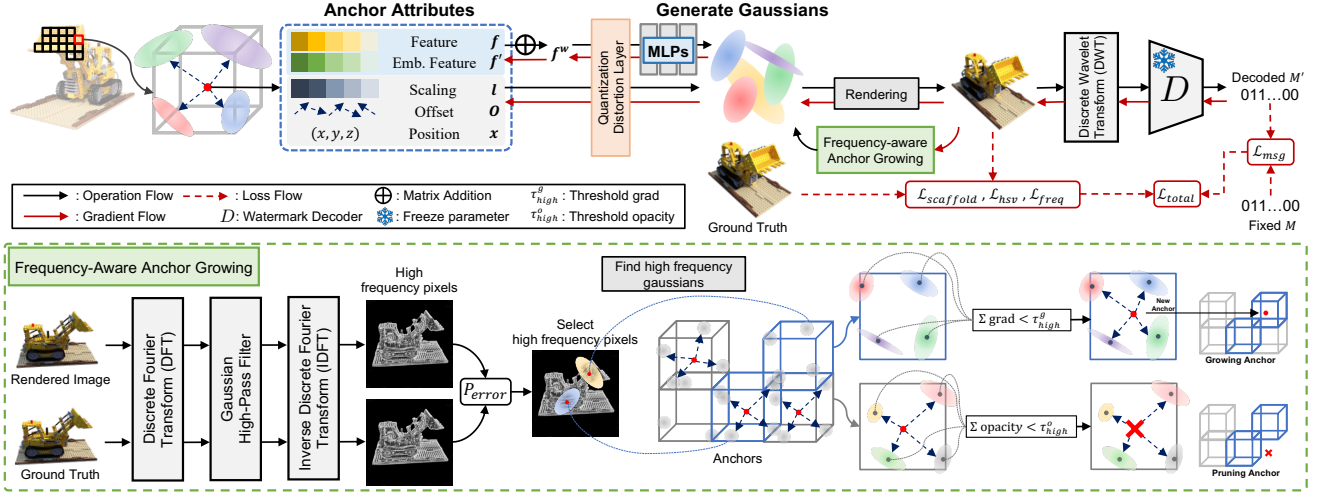


Figure 2. CompMarkGS Overview. We enhance anchor attributes with a watermark embedding feature during training to produce watermarked anchor features. Quantized features from the quantization distortion layer are fed into individual MLPs to predict Gaussian attributes. The rendered image undergoes a discrete wavelet transform to extract low-frequency components for watermark extraction via a pre-trained decoder. During training, frequency-aware anchor growing is applied in high-frequency regions, while image quality is further improved using an HSV loss \mathcal{L}_{hsv} and a frequency loss \mathcal{L}_{freq} . Finally, the entire model is optimized using a total loss \mathcal{L}_{total} .

specific, we leverage the quantization technique used in anchor-based 3DGS compression [4, 40] to inject quantization noise into the watermarked anchor feature f^w during training. This approach prevents the loss of watermark information during subsequent quantization-based compression. The quantization computation is performed as follows:

$$\tilde{f}_i^w = f_i^w + \mathcal{U}\left(-\frac{1}{2}, \frac{1}{2}\right) \cdot q_i, \\ \text{where } q_i = Q_0 \cdot \left(1 + \tanh(r_i)\right), \\ r_i = \text{MLP}_q(f_i^w) \quad (6)$$

where q denotes the quantization step, and r is the refinement output from an MLP_q that takes f^w as input, used to adjust the initial quantization step Q_0 . Thus, by scaling a randomly generated d -dimensional noise vector from a uniform distribution over $[\frac{1}{2}, \frac{1}{2}]$ by a q and adding it to the watermarked anchor feature f^w , we simulate the rounding error caused by quantization, thereby reflecting the effects of quantization during training. In this process, q is learnable.

As shown in Fig.2, the quantized watermarked anchor feature \tilde{f}^w is processed through individual MLPs to predict Gaussian attributes and subsequently undergoes rendering. According to WaterRF [10], embedding the message in the spatial domain is vulnerable to attacks that distort the spatial domain, such as JPEG compression and cropping. Therefore, to achieve robust watermarking against spatial domain attacks, we embed the watermark into the low-frequency region. To this end, we extract the low-frequency components using the Discrete Wavelet Transform (DWT). Although DWT subbands can be computed across multiple levels,

higher levels introduce significant distortion; thus, we employ a one-level DWT, which decomposes the image into four subbands (LL, LH, HL, HH). The low-frequency LL subband of the rendered images, I_{LL} , are then used as the inputs to a pre-trained HiDDen [50] decoder D to extract the watermark message M' :

$$M' = D(I_{LL}), \quad (7)$$

4.3. Frequency-Aware Anchor Growing

As discussed in the above section (Sec. 4.2), we embed the watermark in the low-frequency region to improve robustness against spatial domain attacks. However, because the low-frequency region represents the overall structure of the image, watermark embedding in this area can alter the low-frequency information, subtly changing the global structure and potentially causing blurred boundaries or slight distortions in the texture. Conventional anchor growing methods designate Gaussians with significant gradient changes as new anchors over the training iterations, uniformly distributing anchors without region-specific processing, which may lead to detail loss. To address this issue, we propose a frequency-aware anchor growing method that performs anchor growing in high-frequency regions containing detailed information such as textures. As illustrated in Fig.2, the rendered image I' and the ground truth image I are first transformed into the frequency domain using the Discrete Fourier Transform (DFT).

To isolate the high-frequency components, we generate a Gaussian high-pass mask G_{mask} by assigning weights based on the Euclidean distance between the pixel location and the center of the image, suppressing the low-frequency

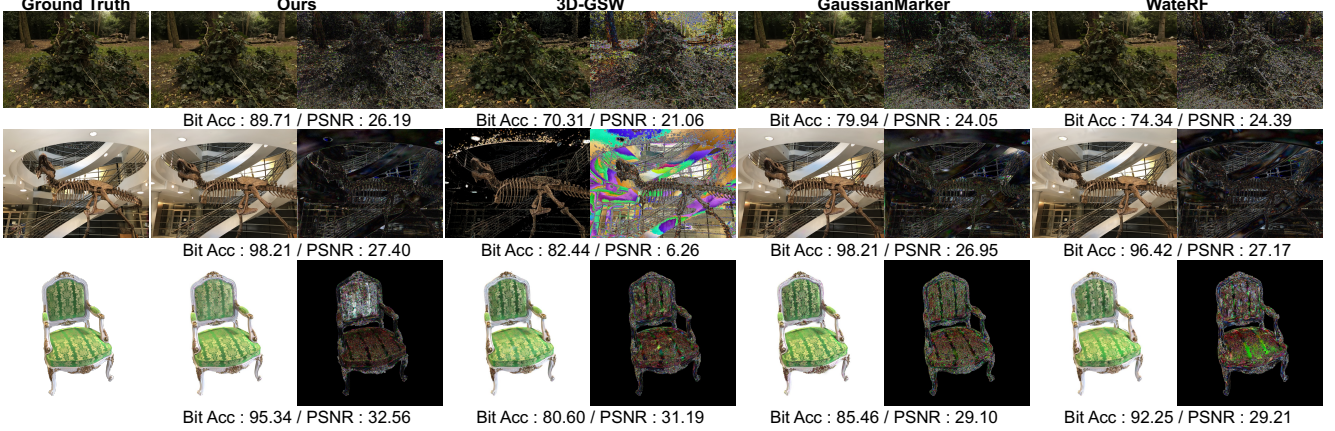


Figure 3. Comparison of image quality after compression between our method and baselines. For each method, the left image is the rendered image, and the right is the difference map, magnified five times. This result is based on 48-bit messages. Our method achieves the best bit accuracy and rendered image quality.

components and emphasizing the high-frequency details.

$$G_{mask}(p) = 1 - \exp\left(-\frac{(d(p) - \tau)^2}{2\beta}\right), \quad (8)$$

where $d(p)$ denotes the distance of a pixel coordinate p from the center of the image, τ and β are parameters that control the mask's cutoff threshold and attenuation degree, respectively. The generated mask $G_{mask}(p)$ at a pixel coordinate p is then multiplied to the corresponding value of the Fourier-transformed image to suppress low-frequency components and preserve high-frequency ones. Finally, an inverse Fourier transform is performed to reconstruct the filtered image in the spatial domain, yielding high-frequency enhanced images I'_{hf} . Subsequently, we define the pixel-wise SSIM loss at each pixel as follows:

$$P_{error}(p) = 1 - \text{SSIM}(I_{hf}(p), I'_{hf}(p)), \quad (9)$$

where $I'_{hf}(p)$ denotes a pixel value in the high-frequency region of the rendered image, while $I_{hf}(p)$ corresponds to a pixel value in the high-frequency region of the ground truth image. After computing the median of all pixel-wise SSIM losses, denoted as \tilde{P}_{error} , we select pixels within the range $[\tilde{P}_{error} - \epsilon, \tilde{P}_{error} + \epsilon]$ to create a binary mask, which is then used to extract the 2D coordinates of pixels in the high-frequency region. Simultaneously, each 3D Gaussian is projected onto the 2D image plane, and the projected 2D position parameters are rounded to obtain pixel-level coordinates. We match these 2D Gaussian coordinates with the high-frequency pixel coordinates using a hash function that maps 2D coordinates to one-dimensional indices. Specifically, each pixel's index is computed as the product of its row index and image width plus its column index, with the same mapping applied to the high-frequency coordinates. By comparing these indices, we generate a boolean mask

F_{mask} that identifies anchors located in the high-frequency region. The Gaussians selected by F_{mask} are then considered active for the anchor growing process. Additional details on anchor growing are provided in the supplementary.

4.4. Objective Function

Wateramrk Message Loss. For training our approach, the watermarked anchor features are processed by individual MLPs to predict Gaussian attributes and render the scene. As mentioned in the previous sections, to embed the watermark in the low-frequency domain, the rendered images are processed using a Discrete Wavelet Transform(DWT) to extract the low-frequency components. These images are then input to a pre-trained HiDDen [50] decoder to output the watermark message, M' , and the watermark message loss \mathcal{L}_{msg} is defined as a Binary Cross Entropy(BCE) loss:

$$\begin{aligned} \mathcal{L}_{msg} = & - \sum_{i=1}^L M_i \log(\sigma(M'_i)) \\ & + (1 - M_i) \log(1 - \sigma(M'_i)), \end{aligned} \quad (10)$$

where $M \in \{0, 1\}^L$ is the ground truth message, and a sigmoid function σ constrains M' to $[0, 1]$.

HSV Loss. To minimize distortion during watermark embedding, we incorporate the \mathcal{L}_{hsv} and \mathcal{L}_{freq} loss terms. Prior studies typically compute image loss in the RGB space to enhance image quality. However, since the RGB space calculates loss based on independent pixel-level color information, it does not accurately reflect human color perception. Therefore, we compute image loss in the HSV space, which represents colors in a manner more similar to the hu-

Methods	Bit Accuracy(%) \uparrow	PSNR \uparrow	SSIM \uparrow	LPIPS \downarrow	Size(MB) \downarrow
HAC [4] + WateRF [10]	91.02 / 54.40	<u>27.36</u> / <u>13.63</u>	<u>0.850</u> / 0.457	<u>0.174</u> / 0.574	<u>207.72</u> / 13.66
HAC [4] + GaussianMarker [9]	<u>92.00</u> / <u>58.34</u>	27.05 / 13.54	<u>0.840</u> / <u>0.460</u>	<u>0.193</u> / <u>0.571</u>	341.30 / 24.33
HAC [4] + 3D-GSW [11]	90.96 / 46.52	19.57 / 13.13	0.628 / 0.439	0.295 / 0.572	173.64 / <u>12.93</u>
HAC [4] + CompMarkGS	95.95 / 95.92	27.68 / 27.65	0.856 / 0.852	0.171 / 0.177	208.96 / 12.23
ContextGS [40] + WateRF [10]	<u>92.01</u> / <u>90.36</u>	26.64 / 26.47	<u>0.843</u> / <u>0.832</u>	<u>0.183</u> / <u>0.185</u>	219.48 / 9.88
ContextGS [40] + GaussianMarker [9]	91.24 / 87.95	<u>26.89</u> / <u>26.54</u>	0.839 / 0.827	0.195 / 0.200	342.38 / 17.86
ContextGS [40] + 3D-GSW [11]	88.28 / 79.75	19.50 / 19.83	0.627 / 0.617	0.294 / 0.299	<u>177.19</u> / <u>9.24</u>
ContextGS [40] + CompMarkGS	94.36 / 94.03	27.60 / 27.55	0.845 / 0.844	0.172 / 0.173	73.39 / 5.72

Table 1. Quantitative comparison of before and after compression bit accuracy and rendering quality. Evaluations were performed using a 48-bit setting, averaged over the Blender, LLFF, and Mip-NeRF 360 datasets. Baselines were tested within an anchor-based 3DGS framework with HAC and ContextGS compression. The best and second-best results are in **bold** and underlined, respectively.

Methods	Bit Accuracy(%) \uparrow						
	No Distortion	Gaussian Noise ($\sigma = 0.1$)	Rotation ($\pm\pi/6$)	Scaling (75%)	Gaussian Blur ($\sigma = 0.1$)	Crop (40%)	JPEG Compression (50% quality)
HAC [4] + WateRF [10]	91.02 / 54.40	<u>89.75</u> / 55.90	<u>84.92</u> / 56.16	86.17 / 55.38	<u>89.33</u> / 56.34	<u>87.00</u> / 55.30	<u>84.00</u> / 57.47
HAC [4] + GaussianMarker [9]	<u>92.00</u> / <u>58.34</u>	59.08 / <u>58.33</u>	58.75 / <u>58.33</u>	58.33 / <u>58.33</u>	59.08 / <u>58.33</u>	61.42 / <u>58.17</u>	58.25 / <u>58.33</u>
HAC [4] + 3D-GSW [11]	90.96 / 46.52	89.50 / 47.50	86.67 / 47.75	<u>86.42</u> / 47.92	86.67 / 47.75	86.92 / 52.50	83.83 / 46.75
HAC [4] + CompMarkGS	95.95 / 95.92	96.00 / 95.50	92.25 / 92.08	91.83 / 91.67	95.83 / 95.58	90.67 / 90.83	87.75 / 88.83
ContextGS [40] + WateRF [10]	<u>92.01</u> / <u>90.36</u>	<u>92.25</u> / <u>91.50</u>	<u>88.75</u> / <u>88.00</u>	<u>89.58</u> / <u>88.83</u>	<u>92.75</u> / <u>91.50</u>	<u>89.50</u> / <u>88.25</u>	86.41 / <u>84.58</u>
ContextGS [40] + GaussianMarker [9]	91.24 / 87.95	59.08 / 58.92	59.00 / 58.75	58.25 / 58.17	59.17 / 58.92	61.08 / 60.67	58.25 / 58.25
ContextGS [40] + 3D-GSW [11]	88.28 / 79.25	87.92 / 80.67	85.08 / 78.75	84.42 / 77.08	88.00 / 81.42	84.33 / 78.50	81.58 / 72.58
ContextGS [40] + CompMarkGS	94.36 / 94.03	93.04 / 92.98	90.17 / 90.33	90.46 / 90.06	92.96 / 92.81	89.63 / 89.29	<u>85.21</u> / 85.31

Table 2. Robustness to image distortion. We compare bit accuracy under various image distortion attacks against baseline methods. The results are averaged over the Blender, LLFF, and Mip-NeRF 360 datasets. Experiments are conducted using 48-bit messages. The best and second-best results are in **bold** and underlined, respectively.

man visual system:

$$\mathcal{L}_{hsv} = \frac{1}{|\mathcal{C}|} \sum_{color \in \mathcal{C}} \mathcal{L}_{color}, \quad (11a)$$

$$\mathcal{L}_{color} = \frac{1}{N_c} \sum_{p \in \Omega} M_c(p) \| I(p) - I_{gt}(p) \|^2, \quad (11b)$$

For each target color c , we define a binary mask $M_c(p)$ such that $M_c(p) = 1$ if the hue of pixel p falls within the range H_c for color c and its saturation $S(p)$ and value $V(p)$ exceed a certain threshold. Then, as in Eq.11a, the color loss \mathcal{L}_{color} for color c is computed as the mean squared error (MSE) between the rendered image $I(p)$ and the ground truth $I_{gt}(p)$ over the pixels in the set Ω where $M_c(p) = 1$. The overall color loss is defined as the average of the losses for each target color in the set \mathcal{C} , as shown in Eq.11b.

Total Loss. Additionally, to reduce high-frequency distortions during watermark embedding, we employ \mathcal{L}_{freq} , as the mean of all pixel-wise SSIM losses. The overall training loss for our method is given by:

$$\mathcal{L}_{total} = \lambda_{img} (\mathcal{L}_{scaffold} + \lambda_{hsv} \mathcal{L}_{hsv} + \lambda_{freq} \mathcal{L}_{freq}) + \lambda_{msg} \mathcal{L}_{msg} \quad (12)$$

where $\mathcal{L}_{scaffold}$ represents the reconstruction loss from the original Scaffold-GS, with details in supplementary.

5. Experiments

5.1. Experimental Setting

Datasets. Following previous works [9, 11], we evaluate our method using the Blender [26], LLFF [25], and Mip-NeRF 360 [3] datasets. We use all 25 scenes: 8 synthetic bounded scenes from the Blender dataset, 8 forward-facing real-world scenes from the LLFF dataset, and 9 bounded real-world scenes from the Mip-NeRF 360 dataset. We assess performance using 200 test images from the Blender dataset. For the LLFF and Mip-NeRF 360 datasets, we adopt the same data split strategy as Mip-NeRF 360

Baselines. We compared our proposed CompMarkGS with three state-of-the-art watermarking techniques applied to anchor-based 3DGS model compression. In our experiments, we evaluated the 3DGS-based methods GaussianMarker [9] and 3D-GSW [11], along with the NeRF-based method WateRF [10], using the anchor-based 3DGS compression methods HAC [4] and ContextGS [40].

Implementation Details. Our method was trained end-to-end on a single A6000 GPU. We conducted experiments for watermark bit-lengths of 32, 48, and 64, focusing on the 48-bit case where we evaluated both before and after compression performance. For the decoder, we pre-trained a HiD-DeN [50] decoder for each bit-length and kept its parame-

ters fixed during watermark training. We used the following parameters: $\lambda_{img} = 10$, $\lambda_{hsv} = 0.6$, $\lambda_{freq} = 0.1$, $\lambda_{msg} = 0.45$. For the quantization step and anchor growing range in high-frequency regions, we set $Q_0 = 1$, $\epsilon = 0.3$.

Methods	Bit Accuracy(%) ↑			
	No Distortion	Gaussian Noise ($\sigma = 0.005$)	Clone (50 %)	Prune (20 %)
WateRF [10]	91.52	81.70	90.23	87.81
GaussianMarker [9]	<u>91.62</u>	73.01	89.83	87.43
3D-GSW [11]	89.62	78.56	88.26	84.84
CompMarkGS	95.16	85.29	94.23	93.32

Table 3. Robustness to model distortion. We show the results on 48-bit, averaged across HAC and ContextGS before quantization compression. The top two results are in **bold** and underlined.

Evaluation. For performance evaluation, we investigated four additional aspects: **1) Fidelity:** We evaluated image quality (PSNR, SSIM, LPIPS) and watermark accuracy before and after compression to verify the preservation of both image fidelity and watermark information. **2) Robustness:** To demonstrate the robustness of our watermark embedding technique, we evaluated watermark bit accuracy and performance metric preservation under six different image distortions and three model distortions. **3) Capacity:** We gradually increased the number of inserted bits from 32 to 48 and 64, recording the corresponding changes in the metrics.

5.2. Experimental results

Fidelity of Before and After Compression. We compared image quality and bit accuracy before and after compression against baseline methods. The compression technique compresses anchor-based 3DGS models using quantization and entropy encoding. As shown in Tab.1, our proposed method exhibits strong robustness to compression. While some baselines achieve higher image quality before compression, conventional methods without the quantization distortion layer suffer significant degradation of watermark and scene information after compression. In particular, the HAC [4]-based method shows the largest performance drop, as existing approaches fine-tune without accounting for both the quantization process and the interpolation required for HAC entropy encoding. Similarly, the ContextGS [40]-based method experiences declines in both bit accuracy and image quality. Moreover, 3D-GSW [11], which performs pruning based on rendering contributions before watermark training, removes both anchors and their associated Gaussians, significantly degrading image quality. These results confirm that our proposed watermarking technique is more suited to model compression than existing methods.

Robustness for the image distortion. We evaluated the robustness of our method against the loss of the embedded watermark when the rendered image is subjected to

Methods	Bit Accuracy(%) ↑		
	32 bits	48 bits	64 bits
WateRF [10]	92.46	91.52	<u>88.21</u>
GaussianMarker [10]	<u>95.07</u>	<u>91.62</u>	79.81
3D-GSW [10]	93.00	89.62	86.31
CompMarkGS	96.52	95.16	91.29

Table 4. Comparison of bit accuracy for our method and baselines at 32, 48, and 64-bit messages, averaged over three datasets, and averaged across HAC and ContextGS before quantization compression. The top two results are in **bold** and underlined.

various distortions. Specifically, we applied six different post-processing techniques to the rendered images: Gaussian Noise ($\sigma = 0.005$), Rotation (random selection within $\pm\pi/6$), Scaling (75% of the original), Gaussian Blur ($\sigma = 0.1$), Crop (40% of the original), and JPEG compression (50% of the original). As shown in Tab.2, We assessed the watermark bit accuracy after post-processing and observed a decrease in bit accuracy, but the performance degradation was relatively smaller than the baselines. These results demonstrate that our proposed watermark embedding technique exhibits strong robustness against image distortion.

Robustness for the model distortion. We evaluated the robustness of our method against direct manipulation of the trained model, which may alter the embedded watermark information. We conducted three model distortion experiments: Gaussian noise ($\sigma = 0.005$), Clone (Randomly clone 50%), and Prune (Randomly remove 20%). Gaussian noise is applied by adding noise with a standard deviation of σ to the model’s parameters while pruning and cloning randomly remove or duplicate anchors, respectively. As shown in Tab.3, we evaluated watermark bit accuracy under various model attacks, and our method demonstrated superior robustness compared to existing approaches. These results confirm that our proposed technique reliably preserves the embedded watermark even when the model itself is subjected to distortion attacks.

Capacity. The number of embedded watermark bits in the rendered image represents a trade-off between image quality and bit accuracy. We conducted experiments using 32, 48, and 64 bits. As shown in Tab.4, increasing the number of embedded watermark bits resulted in a degradation of both image quality and bit accuracy. However, our proposed method show that even with a larger number of bits, the performance degradation is reduced compared to others.

5.3. Ablation Study

Different Combination. We evaluated the effectiveness of Frequency-aware Anchor Growing (FAG), HSV loss, and frequency loss by individually removing each component and measuring image quality and bit accuracy (Tab.5). When FAG was excluded, both image quality and bit accuracy decreased, demonstrating that FAG effectively im-

FAG	\mathcal{L}_{hsv}	\mathcal{L}_{freq}	Bit Acc(%)↑	PSNR ↑	SSIM ↑	LPIPS ↓
-	-	-	<u>94.68</u>	27.53	0.853	0.178
-	-	✓	93.92	27.72	<u>0.855</u>	<u>0.172</u>
-	✓	✓	93.96	<u>27.75</u>	<u>0.855</u>	<u>0.172</u>
✓	✓	✓	95.16	27.64	0.851	0.172

Table 5. Ablation study on the combination of FAG, \mathcal{L}_{hsv} , \mathcal{L}_{freq} with 48-bit messages before quantization compression. We averaged the results across HAC and ContextGS methods.

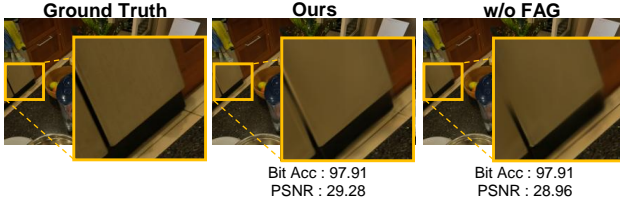


Figure 4. Qualitative comparison of rendered image quality: Ground Truth, Ours w/ FAG, Ours w/o FAG with 48-bit messages.

Target Parameter	Bit Acc(%)↑	PSNR ↑	SSIM ↑	LPIPS ↓
Position	94.44	24.26	0.811	0.211
Scaling	94.06	25.35	0.824	0.207
Offsets	<u>95.72</u>	<u>27.66</u>	<u>0.852</u>	<u>0.174</u>
Anchor Feature (Ours)	95.79	27.78	0.857	0.169

Table 6. Quantitative analysis of watermark embedding into the anchor feature using 48-bit messages, with results presented before quantization compression. We use HAC for the experiment.

proves watermark embedding by increasing the number of anchors in detailed regions prone to distortion. This observation is further confirmed in Fig.4, showing better preservation of fine details when FAG is employed. Additionally, removing HSV loss \mathcal{L}_{hsv} and frequency loss \mathcal{L}_{freq} resulted in significant color distortions, indicating these losses effectively mitigate color degradation during watermark embedding. Lastly, removing all components improved bit accuracy but severely compromised image quality, highlighting the importance of each proposed component.

Watermark Embedding Other Attributes. We compared image quality and bit accuracy when embedding the proposed Watermark Embedding Feature into various anchor attributes such as position, scaling, and offsets. As described earlier, since the Watermark Embedding Feature shares the same dimensions as the anchor feature, we ensured consistency across all attributes before embedding. As shown in Tab.6, embedding the watermark into these attributes results in a performance drop compared to embedding it into the anchor feature. In particular, directly embedding the watermark into parameters that control Gaussian attributes, especially the position parameter representing anchor locations, leads to significant quality degradation. These results show that our proposed method naturally

Methods	Bit Acc(%)↑	PSNR ↑	SSIM ↑	LPIPS ↓
w/o QDL	90.75	26.75	0.844	0.182
w/ QDL	95.92	27.65	0.852	0.177

Table 7. Ablation study comparing our method with and without QDL. Experiments were conducted using 48-bit messages, and results are shown after quantization compression with HAC.

integrates the watermark into the scene’s features without severely compromising the scene’s structural integrity.

Quantization Distortion Layer. We evaluate the robustness of the Quantization Distortion Layer(QDL) in the quantization process. Specifically, we compare image quality and bit accuracy before and after compression with and without QDL. For compression, we employ HAC [4] and ContextGS [40], both of which perform quantization for entropy encoding. As shown in Tab. 7 presents the experimental results for the ContextGS compression method, showing that performance degrades after compression when QDL is not applied. Without QDL, the model fails to adapt to the quantization process during training, leading to significant information loss and reduced bit accuracy during encoding. In contrast, applying QDL enables the model to adapt to quantization during training, thereby minimizing information loss. These results demonstrate that watermarks embedded with QDL exhibit robustness against quantization.

6. Conclusion

We propose CompMarkGS, a lightweight watermarking method for 3DGS, which is a 3DGS watermark method to protect the copyright of the 3DGS model itself while ensuring model efficiency through anchor-based model compression and maintaining high rendering quality. By utilizing learnable watermark embedding features, CompMarkGS naturally integrates watermark information into anchor features, effectively mitigating structural distortions by embedding watermarks as inherent scene attributes. We also introduce a quantization distortion layer to simulate compression during training, minimizing watermark degradation, and propose frequency-aware anchor growing to selectively enhance anchors in high-frequency regions, preserving fine details and rendering quality. HSV loss and frequency loss further mitigate rendering quality degradation. Experimental results demonstrate superior watermark robustness and minimal information loss after compression, providing an effective copyright protection for 3DGS.

Limitations and Future Work. CompMarkGS requires a pre-trained decoder. However, since the decoder needs training only once per bit-length, subsequent usage is efficient without additional fine-tuning. We will extend our method beyond 3DGS compression and develop a lightweight watermarking approach for 3DGS.

References

- [1] Rameen Abdal, Wang Yifan, Zifan Shi, Yinghao Xu, Ryan Po, Zhengfei Kuang, Qifeng Chen, Dit-Yan Yeung, and Gordon Wetzstein. Gaussian shell maps for efficient 3d human generation. In *Proceedings of the IEEE/CVF Conference on Computer Vision and Pattern Recognition*, pages 9441–9451, 2024. [2](#)
- [2] Mauro Barni, Franco Bartolini, and Alessandro Piva. Improved wavelet-based watermarking through pixel-wise masking. *IEEE transactions on image processing*, 10(5):783–791, 2001. [2](#)
- [3] Jonathan T Barron, Ben Mildenhall, Dor Verbin, Pratul P Srinivasan, and Peter Hedman. Mip-nerf 360: Unbounded anti-aliased neural radiance fields. In *Proceedings of the IEEE/CVF conference on computer vision and pattern recognition*, pages 5470–5479, 2022. [6, 3](#)
- [4] Yihang Chen, Qianyi Wu, Weiyao Lin, Mehrtash Harandi, and Jianfei Cai. Hac: Hash-grid assisted context for 3d gaussian splatting compression. In *European Conference on Computer Vision*, pages 422–438. Springer, 2024. [1, 2, 4, 6, 7, 8, 3](#)
- [5] Zilong Chen, Feng Wang, Yikai Wang, and Huaping Liu. Text-to-3d using gaussian splatting. In *Proceedings of the IEEE/CVF conference on computer vision and pattern recognition*, pages 21401–21412, 2024. [2](#)
- [6] Zixuan Chen, Guangcong Wang, Jiahao Zhu, Jianhuang Lai, and Xiaohua Xie. Guardsplat: Robust and efficient watermarking for 3d gaussian splatting. *arXiv preprint arXiv:2411.19895*, 2024. [1](#)
- [7] Jixuan Fan, Wanhu Li, Yifei Han, and Yansong Tang. Momentum-gs: Momentum gaussian self-distillation for high-quality large scene reconstruction. *arXiv preprint arXiv:2412.04887*, 2024. [2](#)
- [8] Zhiwen Fan, Kevin Wang, Kairun Wen, Zehao Zhu, Dejia Xu, Zhangyang Wang, et al. Lightgaussian: Unbounded 3d gaussian compression with 15x reduction and 200+ fps. *Advances in neural information processing systems*, 37:140138–140158, 2025. [2](#)
- [9] Xufeng Huang, Ruiqi Li, Yiu-ming Cheung, Ka Chun Cheung, Simon See, and Renjie Wan. Gaussianmarker: Uncertainty-aware copyright protection of 3d gaussian splatting. *Advances in Neural Information Processing Systems*, 37:33037–33060, 2025. [1, 3, 6, 7, 2](#)
- [10] Youngdong Jang, Dong In Lee, MinHyuk Jang, Jong Wook Kim, Feng Yang, and Sangpil Kim. Waterf: Robust watermarks in radiance fields for protection of copyrights. In *Proceedings of the IEEE/CVF Conference on Computer Vision and Pattern Recognition*, pages 12087–12097, 2024. [2, 4, 6, 7, 1, 3](#)
- [11] Youngdong Jang, Hyunje Park, Feng Yang, Heejoo Ko, Euijin Choo, and Sangpil Kim. 3d-gsw: 3d gaussian splatting for robust watermarking. In *Proceedings of the IEEE/CVF Conference on Computer Vision and Pattern Recognition*, 2025. [1, 3, 6, 7, 2](#)
- [12] Yuheng Jiang, Zhehao Shen, Penghao Wang, Zhuo Su, Yu Hong, Yingliang Zhang, Jingyi Yu, and Lan Xu. Hifi4g: High-fidelity human performance rendering via compact gaussian splatting. In *Proceedings of the IEEE/CVF conference on computer vision and pattern recognition*, pages 19734–19745, 2024. [2](#)
- [13] Zhengyuan Jiang, Jinghuai Zhang, and Neil Zhenqiang Gong. Evading watermark based detection of ai-generated content. In *Proceedings of the 2023 ACM SIGSAC Conference on Computer and Communications Security*, pages 1168–1181, 2023. [2](#)
- [14] Fares Kahlessenane, Amine Khaldi, Redouane Kafi, and Salah Euschi. A dwt based watermarking approach for medical image protection. *Journal of Ambient Intelligence and Humanized Computing*, 12(2):2931–2938, 2021. [2](#)
- [15] Bernhard Kerbl, Georgios Kopanas, Thomas Leimkühler, and George Drettakis. 3d gaussian splatting for real-time radiance field rendering. *ACM Transactions on Graphics*, 42(4):1–14, 2023. [1, 2, 3](#)
- [16] Martin Kutter, Frederic D Jordan, and Frank Bossen. Digital signature of color images using amplitude modulation. In *Storage and Retrieval for Image and Video Databases V*, pages 518–526. SPIE, 1997. [2](#)
- [17] Joo Chan Lee, Daniel Rho, Xiangyu Sun, Jong Hwan Ko, and Eunbyung Park. Compact 3d gaussian representation for radiance field. In *Proceedings of the IEEE/CVF Conference on Computer Vision and Pattern Recognition*, pages 21719–21728, 2024. [2](#)
- [18] Yonghan Lee, Jaehoon Choi, Dongki Jung, Jaeseong Yun, Soohyun Ryu, Dinesh Manocha, and Suyong Yeon. Modesgs: Monocular depth guided anchored 3d gaussian splatting for robust ground-view scene rendering. *arXiv preprint arXiv:2410.04646*, 2024. [2](#)
- [19] Zhan Li, Zhang Chen, Zhong Li, and Yi Xu. Spacetime gaussian feature splatting for real-time dynamic view synthesis. In *Proceedings of the IEEE/CVF Conference on Computer Vision and Pattern Recognition*, pages 8508–8520, 2024. [2](#)
- [20] Youtian Lin, Zuozhuo Dai, Siyu Zhu, and Yao Yao. Gaussian-flow: 4d reconstruction with dynamic 3d gaussian particle. In *Proceedings of the IEEE/CVF Conference on Computer Vision and Pattern Recognition*, pages 21136–21145, 2024. [2](#)
- [21] Xi Liu, Chaoyi Zhou, and Siyu Huang. 3dgs-enhancer: Enhancing unbounded 3d gaussian splatting with view-consistent 2d diffusion priors. *Advances in Neural Information Processing Systems*, 37:133305–133327, 2024. [2](#)
- [22] Tao Lu, Mulin Yu, Linning Xu, Yuanbo Xiangli, Limin Wang, Dahua Lin, and Bo Dai. Scaffold-gs: Structured 3d gaussians for view-adaptive rendering. In *Proceedings of the IEEE/CVF Conference on Computer Vision and Pattern Recognition*, pages 20654–20664, 2024. [2, 3, 1](#)
- [23] Xiyang Luo, Ruohan Zhan, Huiwen Chang, Feng Yang, and Peyman Milanfar. Distortion agnostic deep watermarking. In *Proceedings of the IEEE/CVF conference on computer vision and pattern recognition*, pages 13548–13557, 2020. [2](#)
- [24] Ziyuan Luo, Qing Guo, Ka Chun Cheung, Simon See, and Renjie Wan. Copynerf: Protecting the copyright of neural radiance fields. In *Proceedings of the IEEE/CVF international conference on computer vision*, pages 22401–22411, 2023. [2](#)

- [25] Ben Mildenhall, Pratul P Srinivasan, Rodrigo Ortiz-Cayon, Nima Khademi Kalantari, Ravi Ramamoorthi, Ren Ng, and Abhishek Kar. Local light field fusion: Practical view synthesis with prescriptive sampling guidelines. *ACM Transactions on Graphics (ToG)*, 38(4):1–14, 2019. [6](#), [3](#)
- [26] Ben Mildenhall, Pratul P Srinivasan, Matthew Tancik, Jonathan T Barron, Ravi Ramamoorthi, and Ren Ng. Nerf: Representing scenes as neural radiance fields for view synthesis. *Communications of the ACM*, 65(1):99–106, 2021. [2](#), [6](#), [3](#)
- [27] Gyeongsik Moon, Takaaki Shiratori, and Shunsuke Saito. Expressive whole-body 3d gaussian avatar. In *European Conference on Computer Vision*, pages 19–35. Springer, 2024. [2](#)
- [28] Mohammad Moosazadeh and Gholamhossein Ekbatanifard. A new dct-based robust image watermarking method using teaching-learning-based optimization. *Journal of Information Security and Applications*, 47:28–38, 2019. [2](#)
- [29] Arthur Moreau, Jifei Song, Helisa Dhamo, Richard Shaw, Yiren Zhou, and Eduardo Pérez-Pellitero. Human gaussian splatting: Real-time rendering of animatable avatars. In *Proceedings of the IEEE/CVF conference on computer vision and pattern recognition*, pages 788–798, 2024. [2](#)
- [30] KL Navaneet, Kossar Pourahmadi Meibodi, Soroush Abbasi Koohpayegani, and Hamed Pirsiavash. Compgs: Smaller and faster gaussian splatting with vector quantization. *European Conference on Computer Vision*, 2024. [2](#)
- [31] KL Navaneet, Kossar Pourahmadi Meibodi, Soroush Abbasi Koohpayegani, and Hamed Pirsiavash. Compgs: Smaller and faster gaussian splatting with vector quantization. In *European Conference on Computer Vision*, pages 330–349. Springer, 2024. [2](#)
- [32] KA Navas, Mathews Cherian Ajay, M Lekshmi, Tammy S Archana, and M Sasikumar. Dwt-dct-svd based watermarking. In *2008 3rd international conference on communication systems software and middleware and workshops (COM-SWARE'08)*, pages 271–274. IEEE, 2008. [2](#)
- [33] Zhiyin Qian, Shaofei Wang, Marko Mihajlovic, Andreas Geiger, and Siyu Tang. 3dgs-avatar: Animatable avatars via deformable 3d gaussian splatting. In *Proceedings of the IEEE/CVF conference on computer vision and pattern recognition*, pages 5020–5030, 2024. [2](#)
- [34] Kerui Ren, Lihan Jiang, Tao Lu, Mulin Yu, Linning Xu, Zhangkai Ni, and Bo Dai. Octree- σ s: Towards consistent real-time rendering with lod-structured 3d gaussians. *arXiv preprint arXiv:2403.17898*, 2024. [2](#)
- [35] Tom Sander, Pierre Fernandez, Alain Durmus, Teddy Furon, and Matthijs Douze. Watermark anything with localized messages. *arXiv preprint arXiv:2411.07231*, 2024. [2](#)
- [36] Jiaxiang Tang, Jiawei Ren, Hang Zhou, Ziwei Liu, and Gang Zeng. Dreamgaussian: Generative gaussian splatting for efficient 3d content creation. *arXiv preprint arXiv:2309.16653*, 2023. [2](#)
- [37] Matthieu Urvoy, Dalila Goudia, and Florent Autrusseau. Perceptual dft watermarking with improved detection and robustness to geometrical distortions. *IEEE Transactions on Information Forensics and Security*, 9(7):1108–1119, 2014. [2](#)
- [38] Ron G Van Schyndel, Andrew Z Tirkel, and Charles F Osborne. A digital watermark. In *Proceedings of 1st international conference on image processing*, pages 86–90. IEEE, 1994. [2](#)
- [39] Henan Wang, Hanxin Zhu, Tianyu He, Runsen Feng, Jianjun Deng, Jiang Bian, and Zhibo Chen. End-to-end rate-distortion optimized 3d gaussian representation. In *European Conference on Computer Vision*, pages 76–92. Springer, 2024. [2](#)
- [40] Yufei Wang, Zhihao Li, Lanqing Guo, Wenhan Yang, Alex C Kot, and Bihan Wen. Contextgs: Compact 3d gaussian splatting with anchor level context model. *arXiv preprint arXiv:2405.20721*, 2024. [1](#), [2](#), [4](#), [6](#), [7](#), [8](#), [3](#)
- [41] Yuxin Wang, Qianyi Wu, Guofeng Zhang, and Dan Xu. Learning 3d geometry and feature consistent gaussian splatting for object removal. In *European Conference on Computer Vision*, pages 1–17. Springer, 2024. [2](#)
- [42] Raymond B Wolfgang and Edward J Delp. A watermark for digital images. In *Proceedings of 3rd IEEE International Conference on Image Processing*, pages 219–222. IEEE, 1996. [2](#)
- [43] Guanjun Wu, Taoran Yi, Jiemin Fang, Lingxi Xie, Xiaopeng Zhang, Wei Wei, Wenyu Liu, Qi Tian, and Xinggang Wang. 4d gaussian splatting for real-time dynamic scene rendering. In *Proceedings of the IEEE/CVF conference on computer vision and pattern recognition*, pages 20310–20320, 2024. [2](#)
- [44] Shuzhao Xie, Weixiang Zhang, Chen Tang, Yunpeng Bai, Rongwei Lu, Shijia Ge, and Zhi Wang. Mesongs: Post-training compression of 3d gaussians via efficient attribute transformation. In *European Conference on Computer Vision*, pages 434–452. Springer, 2024. [2](#)
- [45] Tianyi Xie, Zeshun Zong, Yuxing Qiu, Xuan Li, Yutao Feng, Yin Yang, and Chenfanfu Jiang. Physgaussian: Physics-integrated 3d gaussians for generative dynamics. In *Proceedings of the IEEE/CVF Conference on Computer Vision and Pattern Recognition*, pages 4389–4398, 2024. [2](#)
- [46] Taoran Yi, Jiemin Fang, Junjie Wang, Guanjun Wu, Lingxi Xie, Xiaopeng Zhang, Wenyu Liu, Qi Tian, and Xinggang Wang. Gaussiandreamer: Fast generation from text to 3d gaussians by bridging 2d and 3d diffusion models. In *Proceedings of the IEEE/CVF Conference on Computer Vision and Pattern Recognition*, pages 6796–6807, 2024. [2](#)
- [47] Ye Yuan, Xueteng Li, Yangyi Huang, Shalini De Mello, Koki Nagano, Jan Kautz, and Umar Iqbal. Gavatar: Animatable 3d gaussian avatars with implicit mesh learning. In *Proceedings of the IEEE/CVF Conference on Computer Vision and Pattern Recognition*, pages 896–905, 2024. [2](#)
- [48] Chenhao Zhang, Yuanping Cao, and Lei Zhang. Crossviewgs: Cross-view gaussian splatting for large-scale scene reconstruction. *arXiv preprint arXiv:2501.01695*, 2025. [2](#)
- [49] Xuanyu Zhang, Jiarui Meng, Runyi Li, Zhipei Xu, Jian Zhang, et al. Gs-hider: Hiding messages into 3d gaussian splatting. *Advances in Neural Information Processing Systems*, 37:49780–49805, 2025. [1](#)
- [50] Jiren Zhu, Russell Kaplan, Justin Johnson, and Li Fei-Fei. Hidden: Hiding data with deep networks. In *Proceedings of the European conference on computer vision (ECCV)*, pages 657–672, 2018. [2](#), [4](#), [5](#), [6](#)

- [51] Ruijie Zhu, Yanzhe Liang, Hanzhi Chang, Jiacheng Deng, Jiahao Lu, Wenfei Yang, Tianzhu Zhang, and Yongdong Zhang. Motions: Exploring explicit motion guidance for deformable 3d gaussian splatting. *Advances in Neural Information Processing Systems*, 37:101790–101817, 2025. [2](#)

CompMarkGS: Robust Watermarking for Compression 3D Gaussian Splatting

Supplementary Material

Overview

This supplementary material presents additional details and results on our proposed method as follows:

- Sec. 1 details the implementation of the baselines and our proposed method, CompMarkGS, as well as the compression techniques employed.
- Sec. 2 demonstrates further experimental results and the effectiveness of the Quantization Distortion Layer.
- Sec. 3 presents the results showing how bit accuracy and image quality vary with compression size.
- Sec. 4 visually presents additional comparative experiments and ablation study results.

1. Baseline and Implementation Details

Baseline. We conducted comparative experiments with watermarking techniques based on existing 3D scene representation models, namely WateRF [10], GaussianMarker [9], and 3D-GSW [11]. WateRF is based on NeRF, while GaussianMarker and 3D-GSW are based on 3D Gaussian Splatting (3DGS) [15]. For a fair comparison in the same experimental setting, the watermarking techniques for GaussianMarker and 3D-GSW were applied to anchor-based 3DGS. In addition, the existing methods perform watermark embedding through a fine-tuning process using a pre-trained anchor-based 3DGS. Model compression was carried out using HAC [4] and ContextGS [40], compression techniques for anchor-based 3DGS that employ quantization and entropy encoding, and the performance were evaluated post-compression.

Implementation Details. Our proposed method, CompMarkGS, is an anchor-based 3DGS watermarking approach that performs end-to-end training with HAC and ContextGS. The model trains for 30,000 iterations, with watermark training starting after 20,000 iterations to prevent degradation of the base model’s scene reconstruction performance. The anchor growing process runs from iteration 1,600 to 15,000, beginning with conventional anchor growing before applying Frequency-Aware Anchor Growing for fine-grained anchor expansion. The loss function for watermark training consists of the original anchor-based 3DGS loss $\mathcal{L}_{\text{scaffold}}$ and three additional components: the HSV loss \mathcal{L}_{hsv} , frequency loss $\mathcal{L}_{\text{freq}}$, and message loss \mathcal{L}_{msg} . $\mathcal{L}_{\text{scaffold}}$ serves as the reconstruction loss from the original

Scaffold-GS [22] and is defined as follows:

$$\mathcal{L}_{\text{scaffold}} = \mathcal{L}_1 + \lambda_{\text{SSIM}} \mathcal{L}_{\text{SSIM}} + \lambda_{\text{vol}} \mathcal{L}_{\text{vol}}, \quad (1a)$$

$$\mathcal{L}_{\text{vol}} = \sum_{i=1}^{N_{\text{ng}}} \text{Prod}(s_i). \quad (1b)$$

where \mathcal{L}_{vol} is the volume regularization loss, where N_{ng} denotes the number of neural Gaussians in the scene and $\text{Prod}(\cdot)$ represents the product of values in a vector. Therefore, \mathcal{L}_{vol} encourages neural Gaussians to remain small with minimal overlap. The hyperparameters λ_{SSIM} and λ_{vol} used in the loss calculation are set to 0.2 and 0.001, respectively, as proposed in Scaffold-GS.

Anchor Growing and Anchor Pruning. Unlike 3D Gaussian Splatting (3DGS), which performs densification by cloning and splitting individual Gaussian primitives, Scaffold-GS achieves densification through an anchor growing process. In conventional anchor growing, the average gradient ∇_g of the neural Gaussians within each voxel is computed. If a voxel with $\nabla_g > \tau_g$ lacks an anchor point, a new anchor point is placed at the center of that voxel to facilitate anchor growing. Additionally, in the anchor pruning stage, the opacity values of the neural Gaussians associated with an anchor are accumulated over N training iterations, and if the accumulated opacity does not exceed a predefined threshold, the anchor is removed from the scene.

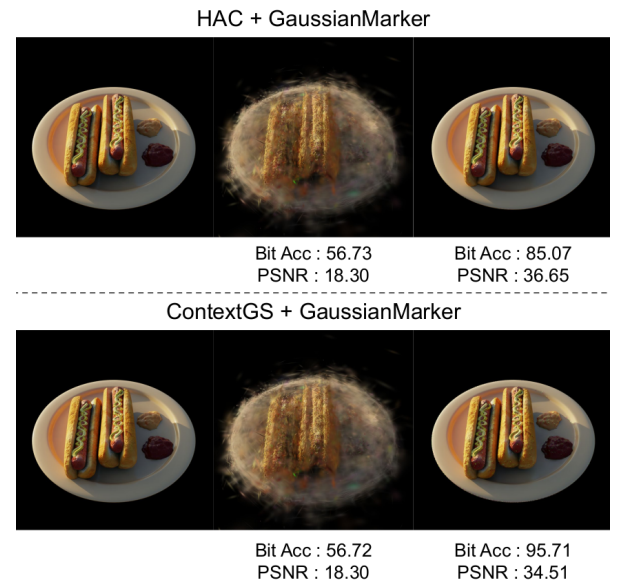


Figure 1. Results for GaussianMarker with and without the Quantization Distortion Layer (QDL). From left to right: Ground Truth, results without QDL, and results with QDL. The evaluation was conducted using 48-bit messages.

2. Quantization Distortion Layer

In the main text, we evaluated our proposed CompMarkGS method with and without the Quantization Distortion Layer (QDL). In this section, we present experiments to examine the impact of applying QDL to existing methods on performance before and after compression. Specifically, we applied QDL to GaussianMarker [9], one of the conventional watermarking techniques, and conducted compression experiments using both HAC [4] and ContextGS [40] schemes. As shown in Fig.1, the results indicate that applying QDL leads to improvements in both image quality and bit accuracy compared to the baseline without QDL. In particular, under the HAC-based compression scheme, the original GaussianMarker without QDL suffers from significant degradation in image quality and bit accuracy after compression, whereas the application of QDL mitigates this performance loss. These findings demonstrate that our proposed QDL effectively reduces watermark information loss during quantization-based compression.

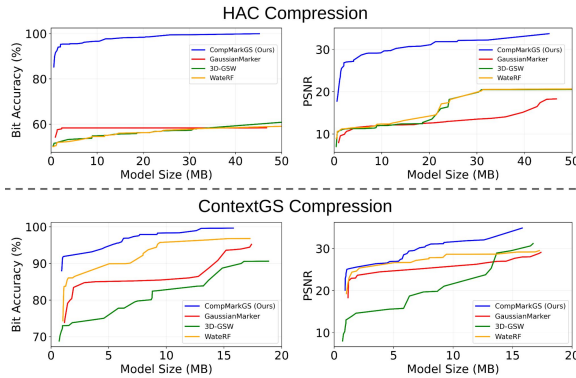


Figure 2. We show the impact of the compression on bit accuracy and image quality. A larger model size corresponds to a lower compression level. The blue line represents our results. Results represent the average score across Blender, LLFF, and Mip-NeRF 360 datasets using 48-bit messages.

3. Performance Across Compression Level

Compression plays a crucial role in determining the trade-off between model size and performance in terms of bit accuracy and image quality. Fig.2 shows the relationship between model size, bit accuracy, and image quality under two different compression: HAC [4] and ContextGS [40]. Fig.2 indicates that a lower compression level leads to better bit accuracy and image quality. Our method consistently outperforms other methods, achieving the highest bit accuracy and image quality across varying model sizes. Notably, for HAC compression, we achieve bit accuracy of 90% with model size less than 10 MB, while other methods only reach 60% under the same model size. These results highlight the effectiveness and robustness of our method.

4. Additional Results

Baseline Comparison. Tab. 1 presents the evaluation of bit accuracy and image quality for each dataset. Our proposed CompMarkGS outperforms existing watermarking methods, such as WaterRF [10], 3D-GSW [11], and GaussianMarker [9], both before and after compression. Under the HAC [4]-based compression scheme, as noted in the previous section, the existing methods do not employ interpolation for quantization and entropy encoding during training. These methods exhibit significantly lower performance than CompMarkGS after compression. Although the performance drop is less pronounced under the ContextGS [40]-based compression scheme, existing methods still experience degradation after compression. These results strongly demonstrate that our approach effectively preserves both watermark durability and overall image quality even in compressed model environments.

Robustness comparison. Fig.3 and Fig.4 show the bit accuracy under varying levels of model distortion. Across different distortion strengths, our proposed method consistently outperforms the baseline. Notably, for prune and clone distortions, our method exhibits less performance degradation, owing to the incorporation of both pruning and anchor growing during training in CompMarkGS. These results indicate that our proposed method achieves superior performance over the baseline even under model distortions.

Qualitative Results. Fig.5 through Fig.13 visualize all results rendered after compression using our method with HAC and ContextGS, along with the difference ($\times 5$) between the original images and the watermarked images.

Methods	Mip-NeRF 360				LLFF				Blender			
	Bit Acc↑	PSNR ↑	SSIM ↑	LPIPS ↓	Bit Acc↑	PSNR ↑	SSIM ↑	LPIPS ↓	Bit Acc↑	PSNR ↑	SSIM ↑	LPIPS ↓
HAC [4] + WateRF [10]	92.27 / 55.24	26.73 / 13.11	0.795 / 0.378	0.253 / 0.660	95.76 / 56.04	25.40 / 10.89	0.811 / 0.452	0.208 / 0.659	84.88 / 51.43	30.01 / 17.43	0.951 / 0.567	0.055 / 0.367
HAC [4] + GM [9]	93.28 / 58.33	26.49 / 13.01	0.777 / 0.379	0.282 / 0.669	96.76 / 58.33	25.39 / 10.25	0.810 / 0.447	0.215 / 0.664	85.82 / 58.36	29.33 / 17.42	0.941 / 0.565	0.073 / 0.367
HAC [4] + 3D-GSW [11]	92.77 / 55.79	18.83 / 12.52	0.669 / 0.373	0.326 / 0.660	95.85 / 55.75	10.44 / 10.41	0.266 / 0.411	0.500 / 0.663	84.04 / 51.40	29.52 / 16.53	0.945 / 0.545	0.056 / 0.380
HAC [4] + CompMarkGS	96.58 / 96.77	27.16 / 26.99	0.808 / 0.798	0.238 / 0.254	98.60 / 98.53	25.32 / 25.29	0.810 / 0.808	0.214 / 0.214	92.61 / 92.35	30.62 / 30.76	0.956 / 0.957	0.054 / 0.053
ContextGS [40] + WateRF [10]	93.02 / 90.92	26.09 / 25.53	0.788 / 0.757	0.260 / 0.260	97.10 / 95.08	25.17 / 25.18	0.809 / 0.809	0.211 / 0.211	85.77 / 85.01	28.73 / 28.80	0.938 / 0.938	0.069 / 0.067
ContextGS [40] + GM [9]	92.49 / 89.65	26.33 / 25.74	0.775 / 0.747	0.282 / 0.289	96.68 / 95.23	25.31 / 25.06	0.811 / 0.806	0.218 / 0.223	84.39 / 78.74	29.10 / 28.91	0.940 / 0.937	0.075 / 0.076
ContextGS [40] + 3D-GSW [11]	91.08 / 83.85	18.53 / 18.71	0.669 / 0.636	0.321 / 0.333	93.49 / 82.57	10.22 / 10.31	0.262 / 0.262	0.503 / 0.507	79.91 / 72.31	29.86 / 30.62	0.949 / 0.952	0.053 / 0.053
ContextGS [40] + CompMarkGS	95.59 / 95.58	26.56 / 26.55	0.777 / 0.776	0.248 / 0.248	98.30 / 98.23	25.60 / 25.57	0.812 / 0.812	0.210 / 0.211	89.04 / 88.02	30.78 / 30.63	0.955 / 0.954	0.050 / 0.051

Table 1. Quantitative comparison of bit accuracy and image quality with baselines before and after compression. In this study, we conduct evaluations at 48-bit and compared performance using the Mip-NeRF360 [3], LLFF [25], and Blender [26] datasets. All baselines were tested within an anchor-based 3DGS framework, employing HAC [4] and ContextGS [40] as the compression methods. The best performance is highlighted in **bold**.

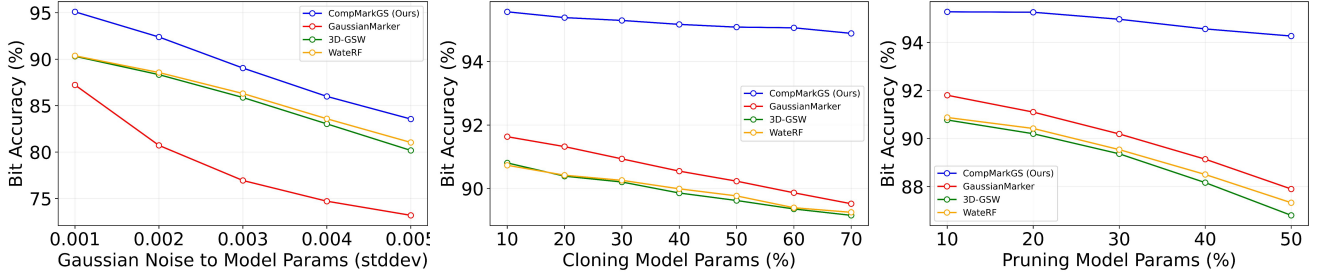


Figure 3. Bit accuracy for WateRF [10], 3D-GSW [11], GaussianMarker [9], and our method for model distortions and distortion strengths. We conduct three model distortions: 1) We add model Gaussian noise to all model parameters. 2) We remove randomly the anchors. 3) We randomly clone the anchors. The blue line represents our results. Our method outperforms other methods. we conducted evaluations at 48-bit and compared performance using the Mip-NeRF360 [3], LLFF [25], and Blender [26] datasets. All baselines were tested within an anchor-based 3DGS framework, employing HAC [4].

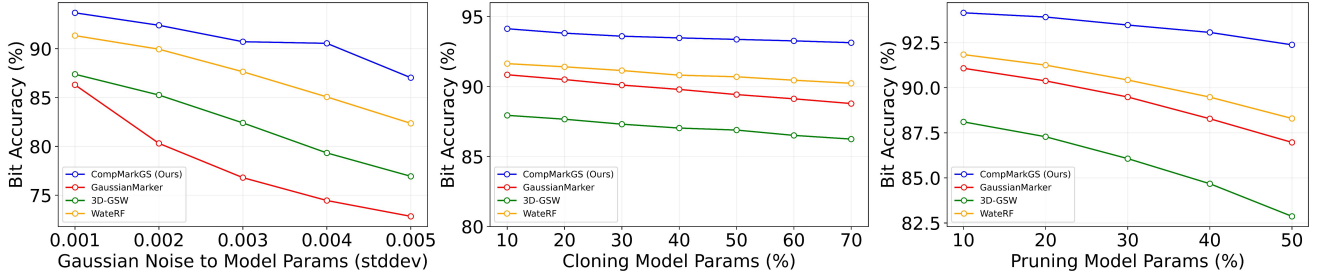


Figure 4. Bit accuracy for WateRF [10], 3D-GSW [11], GaussianMarker [9], and our method for model distortions and distortion strengths. We conduct three model distortions: 1) We add model Gaussian noise to all model parameters. 2) We remove randomly the anchors. 3) We randomly clone the anchors. The blue line represents our results. Our method outperforms other methods. we conducted evaluations at 48-bit and compared performance using the Mip-NeRF360 [3], LLFF [25], and Blender [26] datasets. All baselines were tested within an anchor-based 3DGS framework, employing ContextGS [40].

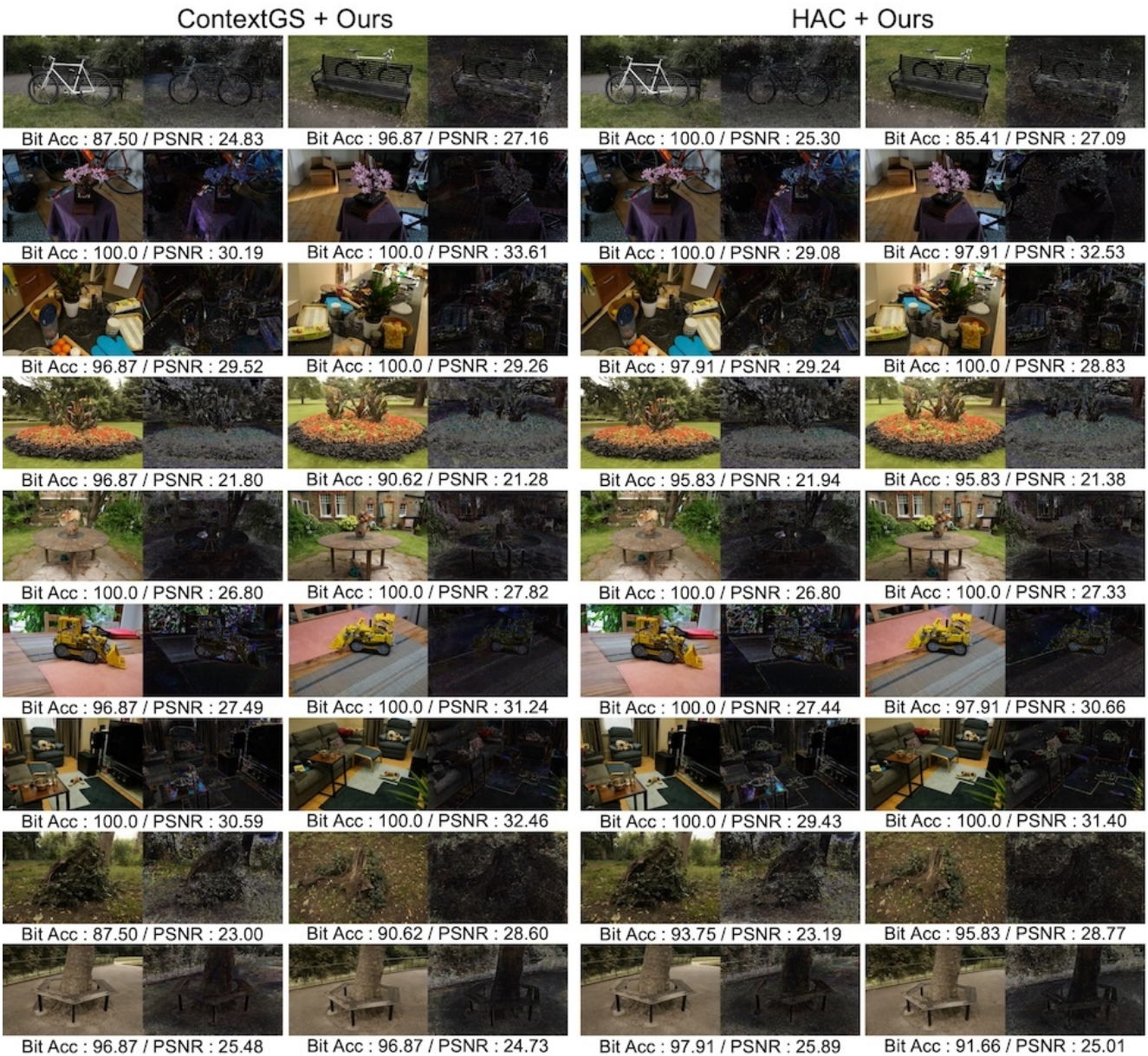


Figure 5. Image quality of various rendering outputs generated by our method on the Mip-NeRF 360 dataset. We show the differences ($\times 5$). The closer is to white, the greater the discrepancy between the ground truth and the rendered image. The results were obtained using a 32-bit configuration after compression.

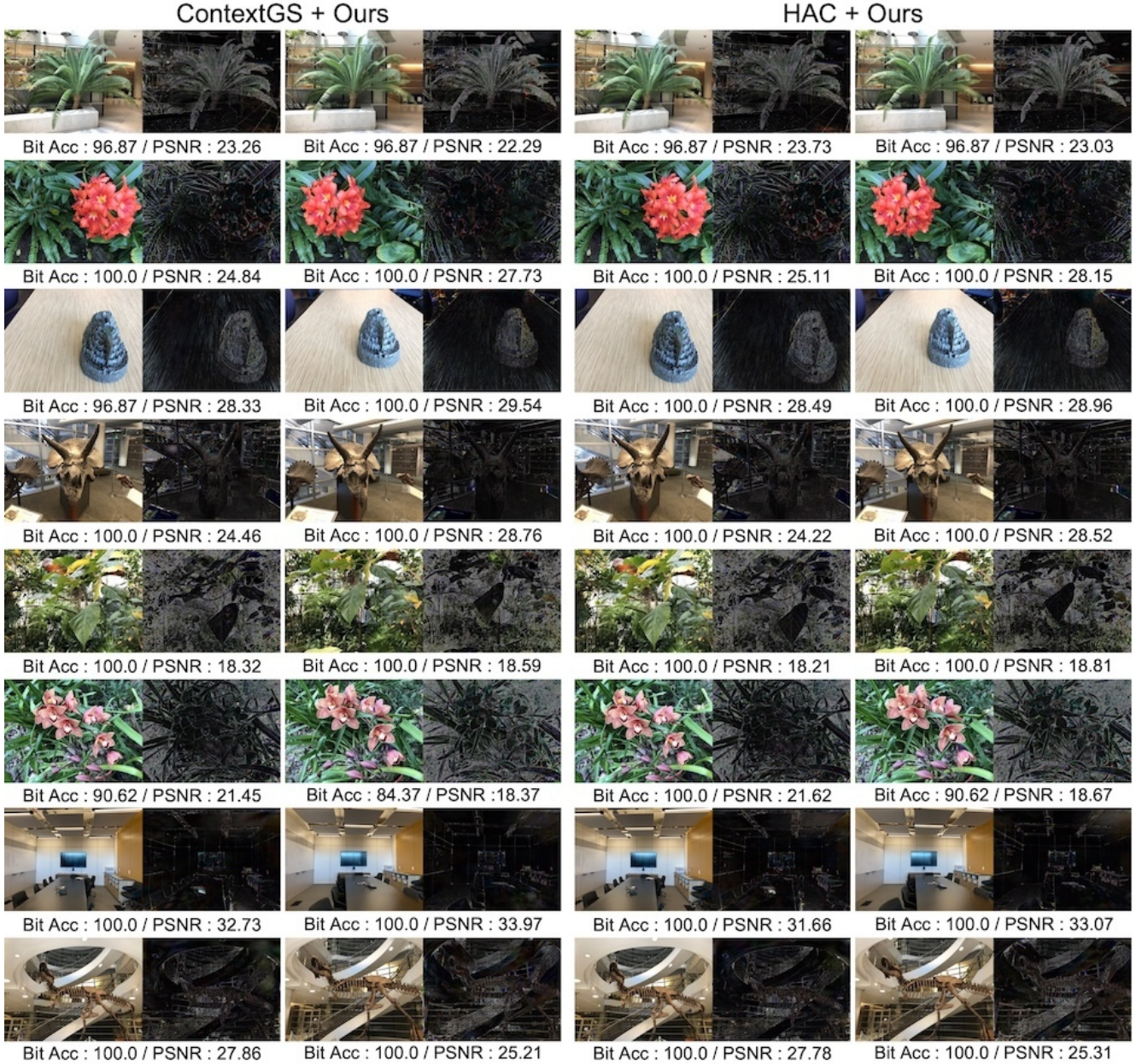


Figure 6. Image quality of various rendering outputs generated by our method on the LLFF dataset. We show the differences ($\times 5$). The closer is to white, the greater the discrepancy between the ground truth and the rendered image. The results were obtained using a 32-bit configuration after compression.

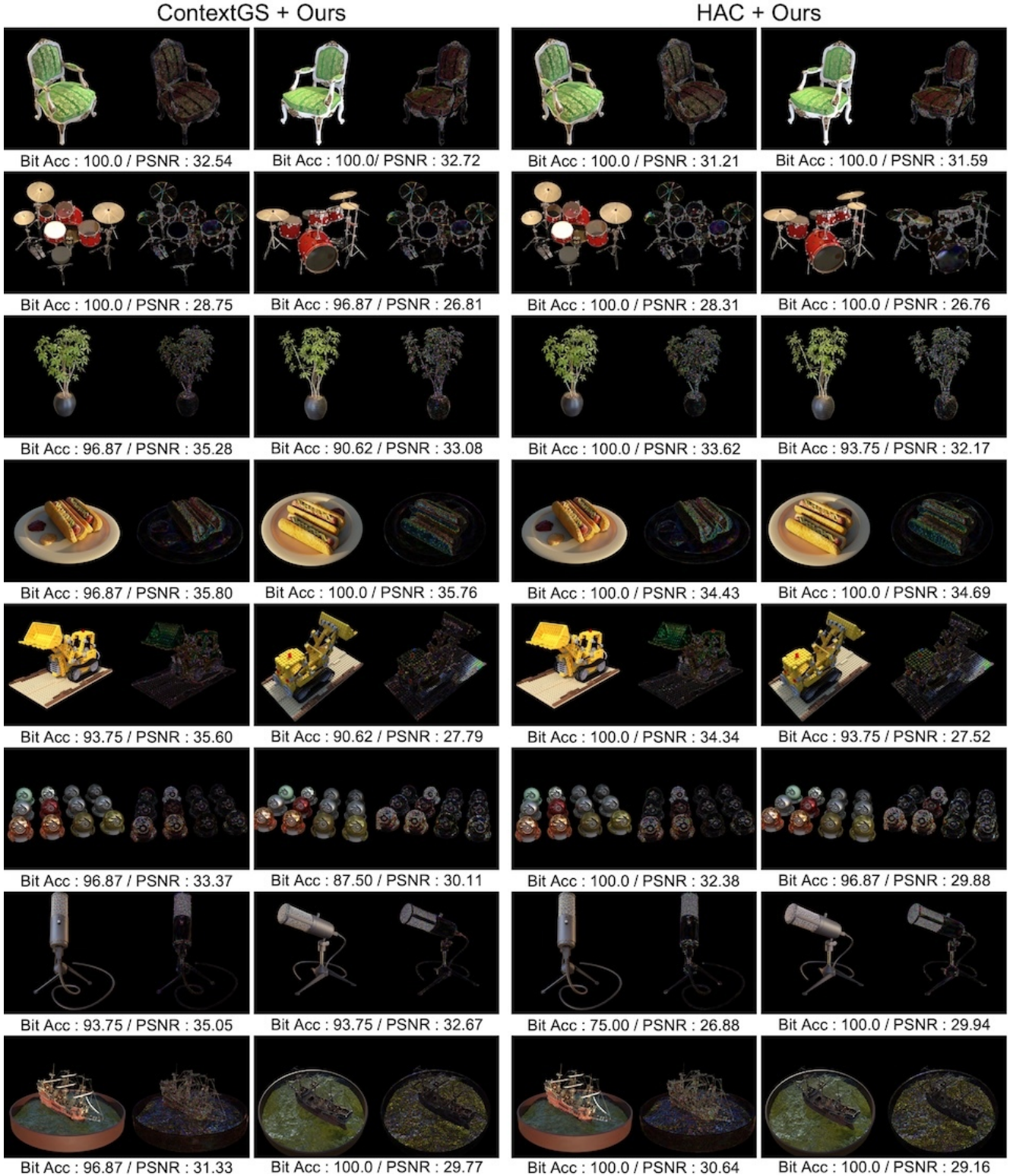


Figure 7. Image quality of various rendering outputs generated by our method on the Blender dataset. We show the differences ($\times 5$). The closer is to white, the greater the discrepancy between the ground truth and the rendered image. The results were obtained using a 32-bit configuration after compression.

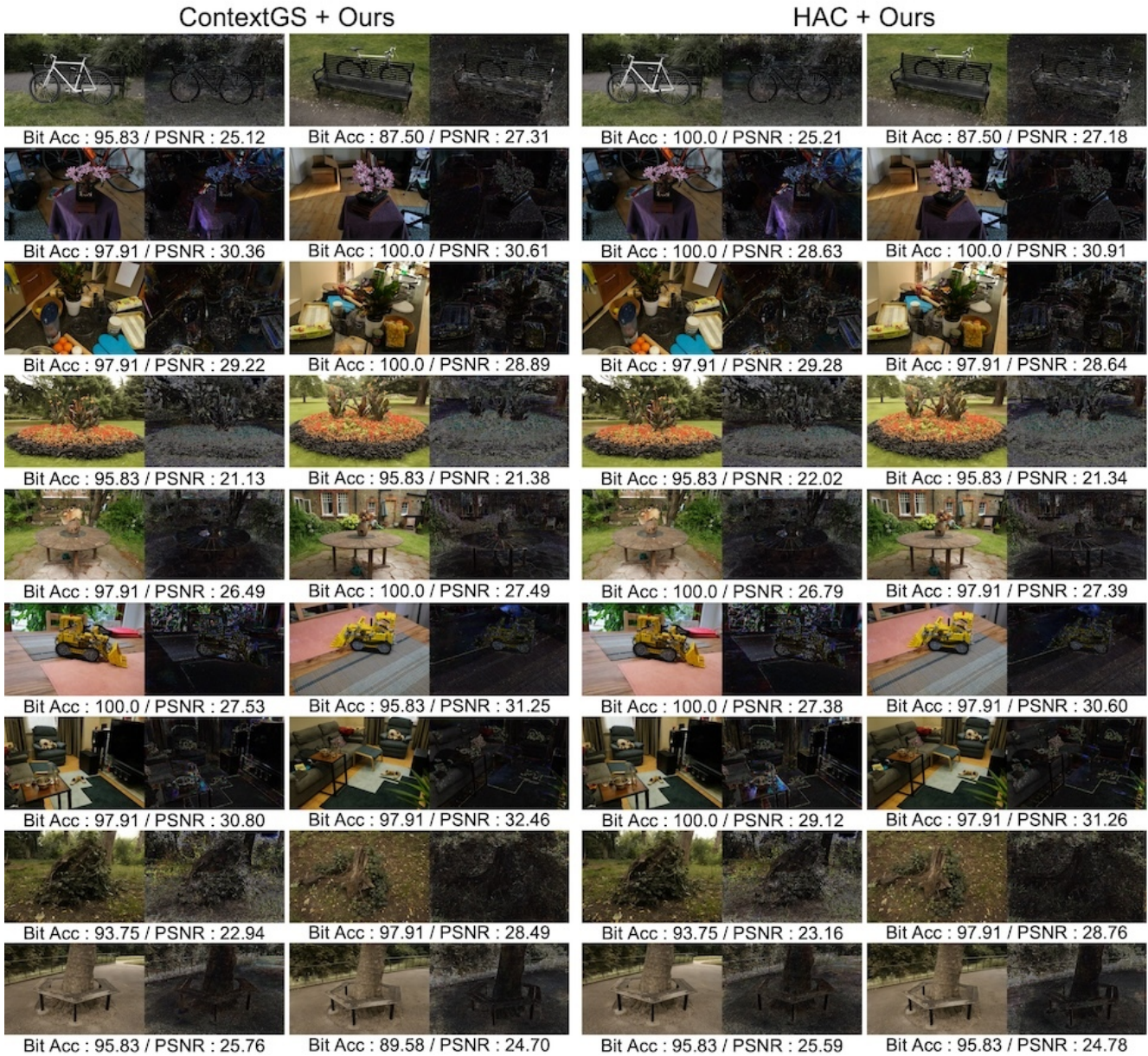


Figure 8. Image quality of various rendering outputs generated by our method on the Mip-NeRF 360 dataset. We show the differences ($\times 5$). The closer is to white, the greater the discrepancy between the ground truth and the rendered image. The results were obtained using a 48-bit configuration after compression.

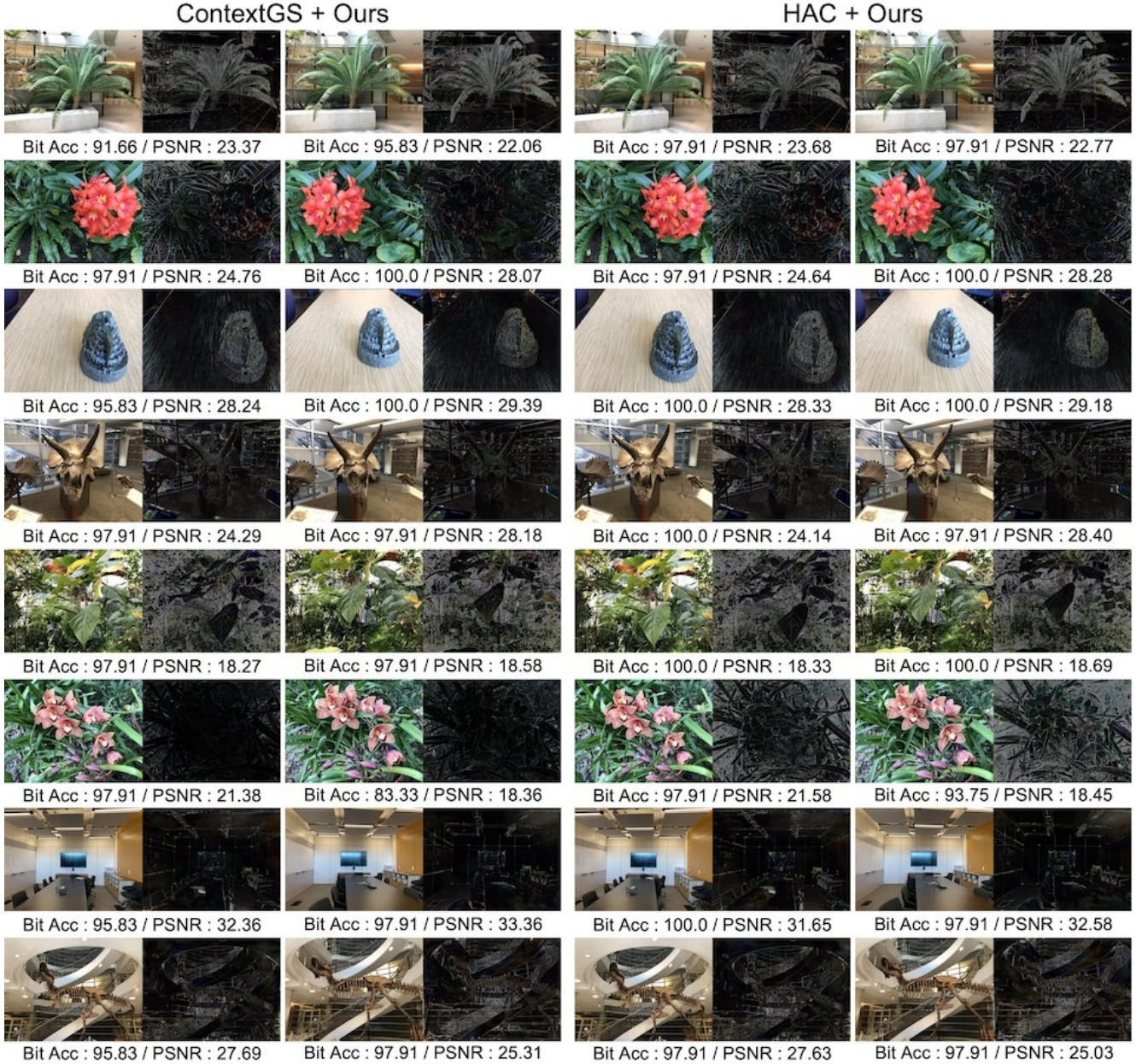


Figure 9. Image quality of various rendering outputs generated by our method on the LLFF dataset. We show the differences ($\times 5$). The closer is to white, the greater the discrepancy between the ground truth and the rendered image. The results were obtained using a 48-bit configuration after compression.

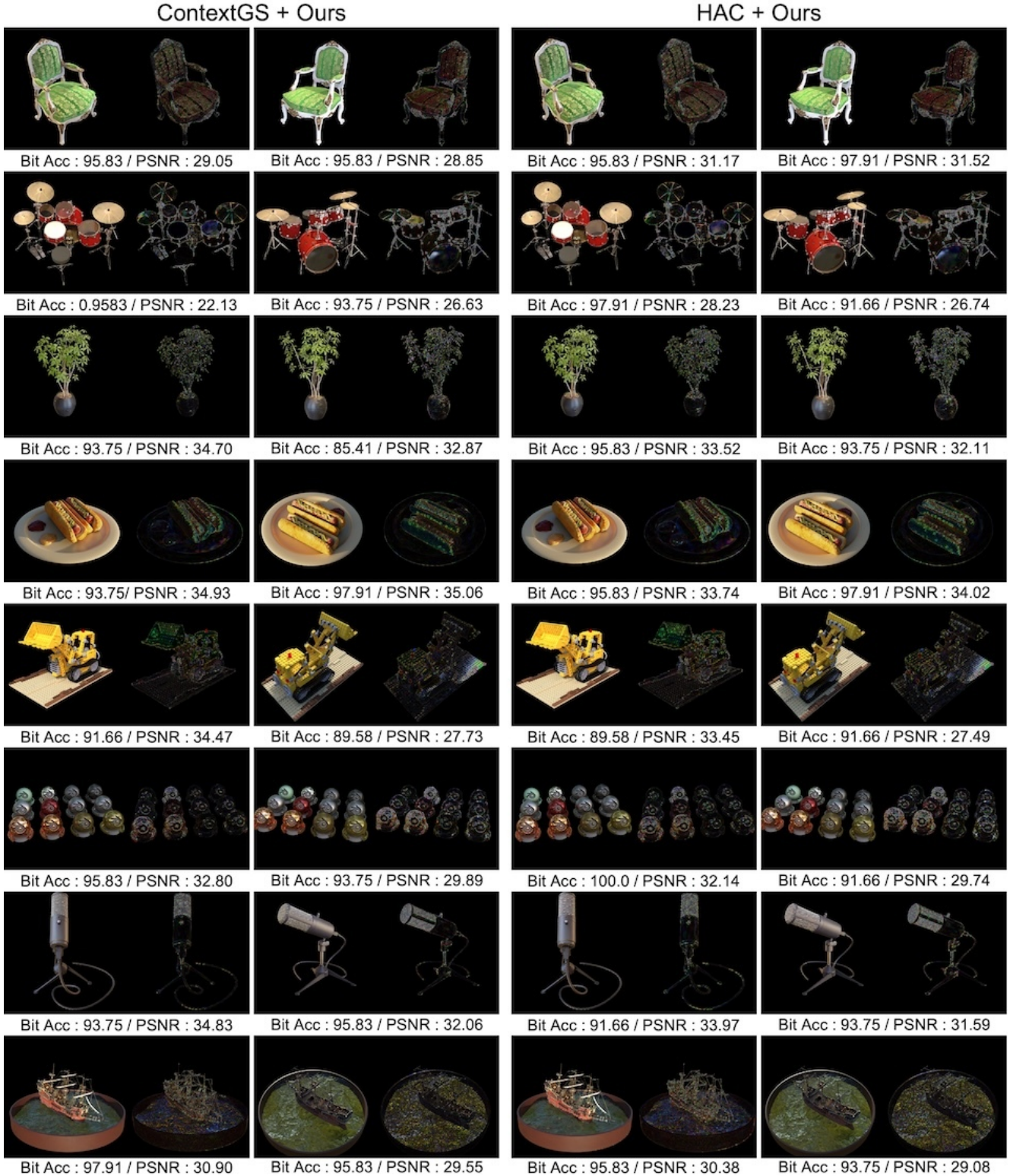


Figure 10. Image quality of various rendering outputs generated by our method on the Blender dataset. We show the differences ($\times 5$). The closer is to white, the greater the discrepancy between the ground truth and the rendered image. The results were obtained using a 48-bit configuration after compression.

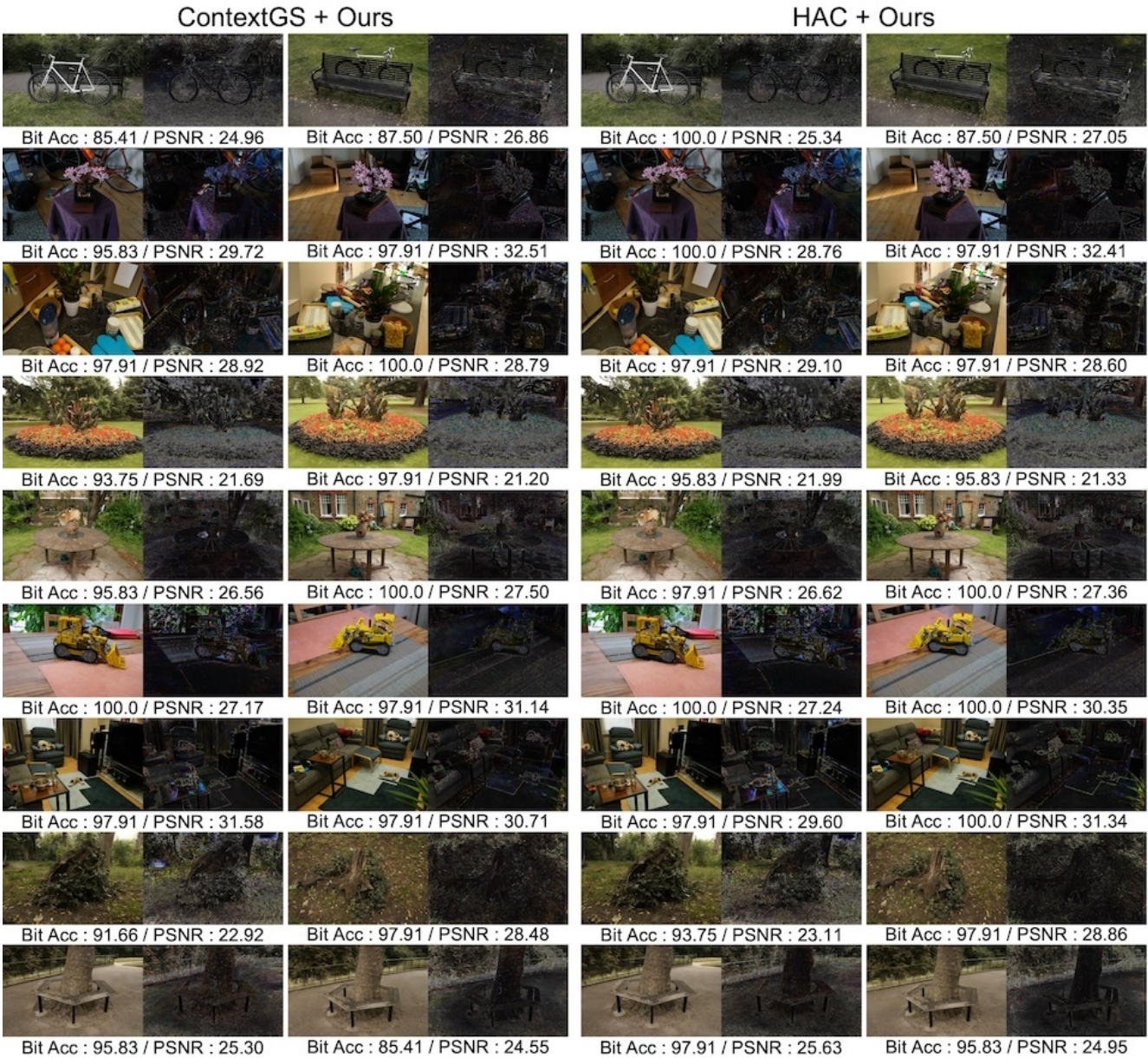


Figure 11. Image quality of various rendering outputs generated by our method on the Mip-NeRF 360 dataset. We show the differences ($\times 5$). The closer is to white, the greater the discrepancy between the ground truth and the rendered image. The results were obtained using a 64-bit configuration after compression.

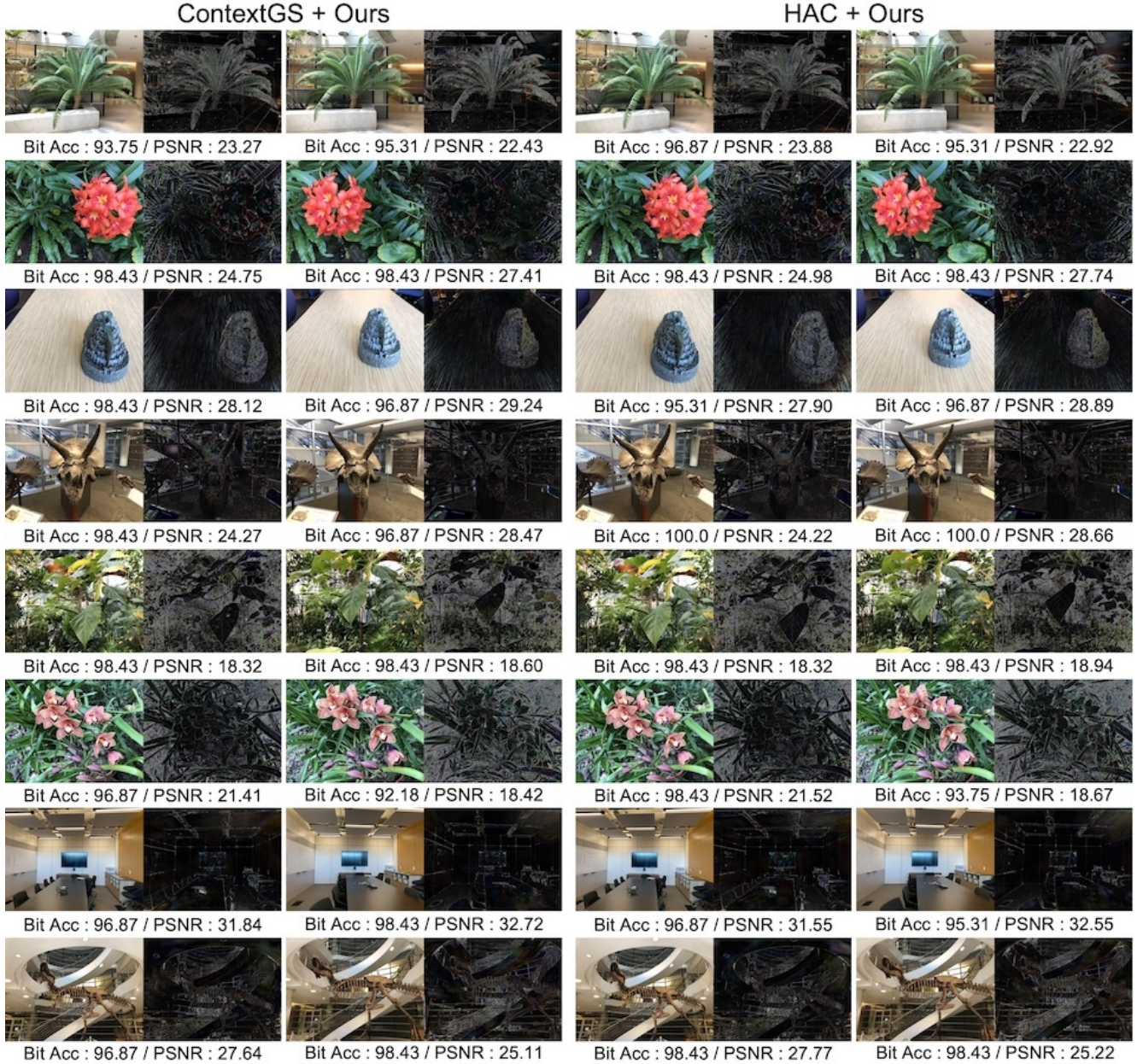


Figure 12. Image quality of various rendering outputs generated by our method on the LLFF dataset. We show the differences ($\times 5$). The closer is to white, the greater the discrepancy between the ground truth and the rendered image. The results were obtained using a 64-bit configuration after compression.

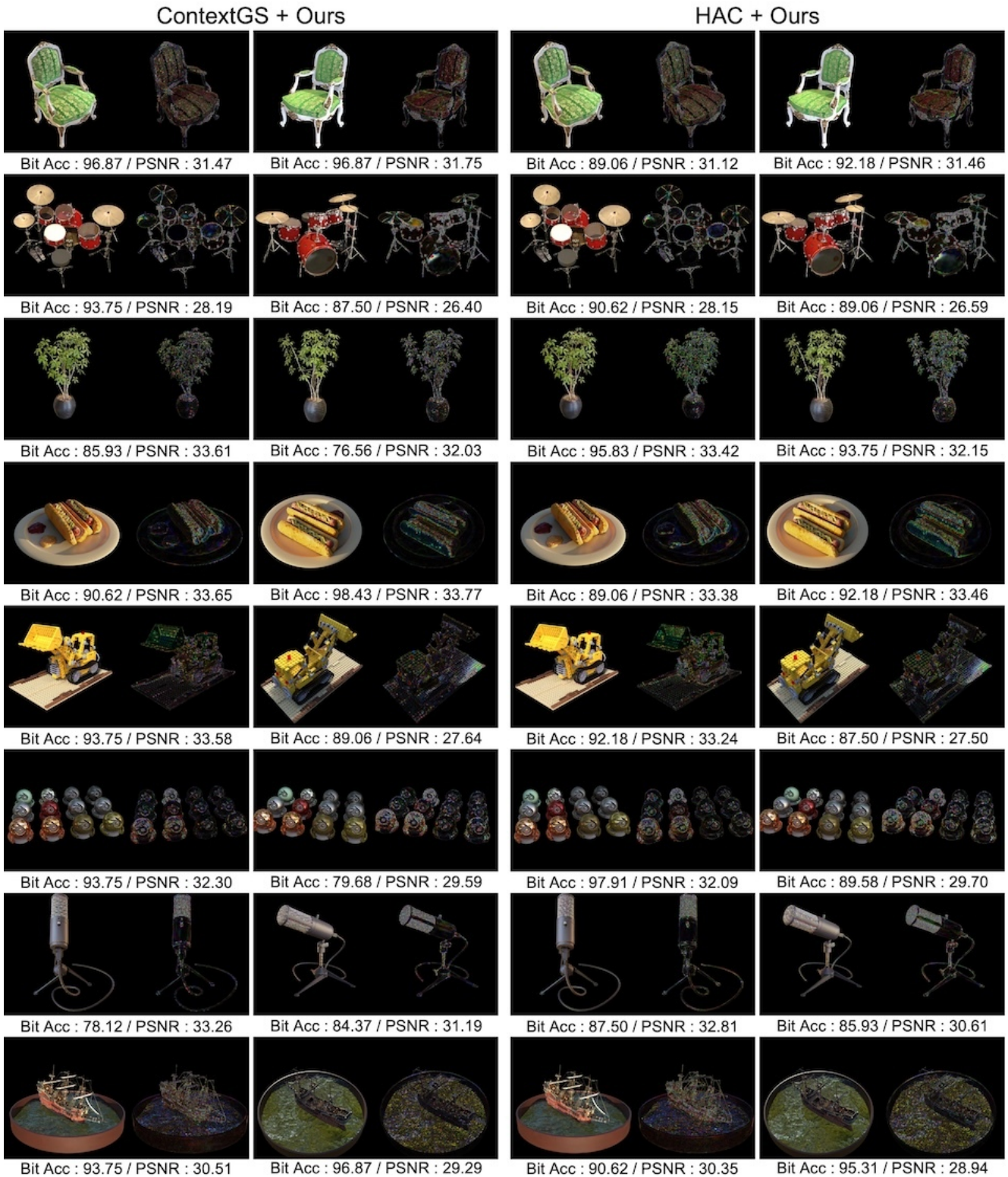


Figure 13. Image quality of various rendering outputs generated by our method on the Blender dataset. We show the differences ($\times 5$). The closer is to white, the greater the discrepancy between the ground truth and the rendered image. The results were obtained using a 64-bit configuration after compression.